

# *DEVELOPMENT OF A BULGE TEST EXPERIMENTAL SETUP*

For the in-situ mechanical characterization of metal thin  
films on polymer substrate



***Politecnico di Milano***

**SCUOLA DI INGEGNERIA**

**MATERIALS ENGINEERING AND NANOTECHNOLOGY**

SUPERVISOR: Prof. PASQUALE VENA

ASSISTANT SUPERVISOR: PhD. EMANUELE CATTARINUZZI

Thesis by:

XUYING XIAN

814984

Academic year: 2015/16

# TABLE OF CONTENTS

ABSTRACT .....	1
<b>1 INTRODUCTION .....</b>	<b>5</b>
1.1 Stretchable electronics .....	5
1.2 Material choice for stretchable electronics .....	9
<u>1.2.1 PDMS as Substrate</u> .....	9
<u>1.2.2 Gold on PDMS</u> .....	10
1.3 Testing methods for thin film properties .....	12
<u>1.3.1 Uniaxial micro tensile test</u> .....	12
<u>1.3.2 Nanoindentation [24] [25]</u> .....	17
<b>2 BULGE TESTING TECHNIQUE: THEORETICAL PRINCIPLES [24].....</b>	<b>22</b>
2.1 Bulge test introduction .....	22
2.2 Bulge equations .....	23
2.3 Circular window model of the bulge test.....	25
2.4 Rectangular window model for bulge test.....	28
2.5 Square Windows.....	31
2.6 Conclusion and discussion.....	33
<b>3 DEVELOPMENT OF THE HYPERELASTIC BULGE EQUATION .....</b>	<b>35</b>
3.1 Basic of hyperelasticity .....	36
3.2 Geometrical general situation.....	39
3.3 Hyperelastic bulge modeling- circular window .....	40
3.4 Hyperelastic bulge modeling- rectangular window.....	41
3.5 Hyperelastic bulge modeling- with constitutive modeling .....	42
<u>3.5.1 Construction of hyperelastic bulge equation with with constitutive models</u> .....	42
<u>3.5.2 Potential usage of the uniaxial hyperelastic equation</u> .....	45
3.6 Conclusion and discussion.....	46
<b>4 DEVELOPMENT OF THE BULGE TEST SETUP .....</b>	<b>47</b>
4.1 Sample preparation [36] .....	48
4.2 Device Manufacture.....	49
<u>4.2.1 Overview of setup</u> .....	49
<u>4.2.2 Cap manufacturing</u> .....	51
<u>4.2.3 Main body manufacturing</u> .....	53
<u>4.2.4 Pressure build up and control</u> .....	55

# TABLE OF CONTENTS

4.3	Specimen preparation and mounting .....	57
5	<b>BULGE TEST WITH IN-SITU LASER PROFILOMETRY .....</b>	<b>59</b>
5.1	Introduction of laser profilometry [38].....	60
5.2	Setup description.....	62
5.3	Experiment Protocol .....	63
5.4	Results and discussion .....	65
5.4.1	<u>Data post-processing and result discussion</u> .....	65
5.4.2	<u>Characterization with hyperelastic model fitting</u> .....	70
6	<b>BULGE TEST WITH IN-SITU OPTICAL MICROSCOPY .....</b>	<b>73</b>
6.1	Setup description.....	74
6.2	Experimental Protocol .....	75
6.3	Results and discussion .....	76
7	<b>CONCLUSION AND RECOMMENDATIONS .....</b>	<b>81</b>
7.1	Thesis Conclusion.....	81
7.2	Conclusion on the experimental setup .....	83
7.3	Advantages and disadvantages of in-situ laser profilometry and in-situ optical microscopy 84	
7.4	Recommendation and future perspectives.....	85
	<b>BIBLIOGRAPHY .....</b>	<b>86</b>

## Abstract

The term *Stretchable Electronics* refers to an emerging research field featuring electronics devices which can be safely bent, stretched and twisted during operation. Matching high deformability and state-of-the-art electronic performances attracts great interest by the industry, since it makes easier to interface electronics with daily life, therefore opening new perspectives in several application fields, namely energy storage, healthcare technology and media communication devices.

Depositing metal thin films (10nm to 10 $\mu$ m thickness range) onto polymeric substrates is one of the most popular strategies to achieve deformable electronic components, with specific reference to stretchable electrical interconnects [1]. Among possible metal/polymer material systems, gold (Au) on Polydimethylsiloxane (PDMS) has its remarkable advantages, namely, extended range of reversible stretchability of the PDMS substrate [2], good conductivity of Au [3] and biocompatibility of both materials [3]. However, it is well known that achieving a reliable deposition of metal upon elastomers is a challenging task [4]. Being the deposition temperature usually in the range of 100°C, the mismatch in thermal expansion coefficient of Au and PDMS makes rise significant residual stresses as the system approaches room temperature [4]. Moreover, plasma-treatment of the polymer surface to enhance subsequent metal/polymer adhesion can cause a significant embrittlement of the polymeric material across a few tenths of nanometers depth from the surface [5]. The combination of the aforementioned phenomena can trigger the onset of undesired cracks, which affect both the metal film and the embrittled layer of the polymer substrate at very limited strains, or even in the undeformed state. Investigation of the cracking behavior of Au/PDMS systems was extensively addressed upon uniaxial strain [6,7]. Nevertheless, the state of biaxial strain is a more realistic deformed condition considering, for instance, the most common applications of stretchable electronics in healthcare technology [8]. Among other testing methods, the bulge testing technique provides significant flexibility in terms of the range of stress/strain states a sample can be subjected to. Following the aforementioned arguments, this study explores the use of the bulge testing the bulge



test method, as an alternative experimental technique to study the cracking behavior of Au/PDMS systems for stretchable electronics applications.

Bulge test is an experimental method suitable for thin film samples and, in brief, it consists in the application of pressure on one side of a sample clamped along the boundaries of a cavity of given shape (from now on referred to as *bulge window*) and in the measurement of the related deflection. Mechanical properties are obtained from the pressure/deflection relationship according to bulge equations, which not only depends on the material properties, while also on the size and shape of the bulge window [9]. Noteworthy, the traditional bulge equation relies on the assumption of linear elastic behavior of the sample, which does not apply to elastomers like PDMS. To overcome this limitation, the first task addressed in this study consists in the development of a reviewed version of the bulge equation, which is described in Chapter 3. The non-linear nature of the constitutive behavior of a typical elastomeric materials was considered. Specifically, the bulge equation was recast in the assumption of incompressible hyperelasticity, for both circular (i.e., equi-biaxial strain) and rectangular (i.e., plane strain) bulge window shapes.

Secondly, the design and manufacture of the bulge test device was addressed. Due the available manufacturing facilities, the circular window shape only was considered, therefore limiting the experimental activity to the equi-biaxial strain case. Material choice and device dimensions were made according to the constraints provided by (i) the manufacturing facilities and (ii) the experimental equipment to be combined with the bulge test device during tests, namely, a laser profilometer and an inverted optical microscope. In chapter 4, the design and manufacturing details are described.

In Chapter 5, a bulge test experiment with in-situ laser profilometry is described. Noteworthy, the bulge window dimension (i.e., 500 $\mu$ m radius) was selected in order to comply with the height-measurement range of the profilometer. This test was devised to gain insight on the bulged sample profiles corresponding to an applied pressure. Besides providing a phenomenological pressure/deflection relationship for a specific bulge device window, experimental results by in-situ profilometry provided the opportunity to infer the constitutive parameters of the PDMS by assuming a specific hyperelastic strain energy potential and by best-fitting the pressure/deflection data

using the hyperelastic bulge equation developed in Chapter 3. Five different hyperelastic strain energy potentials were tested. Based on best-fitting results, a Yeoh strain energy potential [10] was selected to model the PDMS behavior and predict the pressure/deflection relationship for an arbitrary window size.

In Chapter 6, the use of in-situ optical microscopy (20X magnification objective) combined with bulge testing for two different window sizes (namely, 500 $\mu\text{m}$  and 1000 $\mu\text{m}$  radii), is described. Image sequences of crack opening under controlled increasing pressure were obtained. Crack opening evolution was studied by manually measuring the width of 5 cracks at each acquired image. Making use of the hyperelastic bulge equation informed with the best-fitting material parameters described in Chapter 5, the crack opening evolution was plotted against the sample strain. Since results were shown to be independent on the window size of the bulge test device, in Chapter 7 the value provided by the experimental procedure devised in this thesis is discussed making use of the following arguments:

Considering (i) the inherent out-of-plane nature of the bulged profile and (ii) the limited depth of field of the microscope objective, bigger window dimensions maximize the region of the Field of View in sharp focus, when imaging the top of the bulged profile during an experiment with in-situ optical microscopy. In this view, a 1000 $\mu\text{m}$  window should be preferred to a 500 $\mu\text{m}$  one.

On the other hand, as discussed in Chapter 5, the available laser profilometry equipment wasn't suitable for window sizes bigger than 500 $\mu\text{m}$ . Therefore, the hyperelastic bulge equation developed in Chapter 3 provides the opportunity to

- Perform a mechanical characterization in equi-biaxial strain state (indeed, also in plane strain, although it was not explored in terms of experimental activity);
- Predict the pressure/deflection relation of an arbitrary bulge window size once the material parameters are known by previous characterization. The requirement of an in-situ profilometry experiment corresponding to a specific bulge window size is then relaxed, with significant reduction of man-time consumption needed to obtain a description of the crack opening evolution against the strain level.

Although results were promising, some aspects of the experimental activity devised in this thesis can be improved. In Chapter 7, possible future perspectives are discussed, namely,

- The fabrication of the bulge test device making use of manufacturing tools featuring higher precision (e.g., 10 $\mu\text{m}$  rather than the current 100 $\mu\text{m}$ );
- The development of an automated procedure for the measurement of the crack opening at increasing strain.

# 1 Introduction

## 1.1 Stretchable electronics

Though the main tendency of study in electronics area is still to achieve faster and smaller devices as rigid planar circuits, one cannot neglect the limitation of a stiff structure when interfacing with curved or even soft surfaces. Stretchable electronics, on the other hand, has been demonstrated as a technology that can negotiate high deformability and state-of-the-art electronic performances, thus it is becoming a new trend of research. It has significant prospective application, especially in the biomedical field, for example, skin-like sensors, flexible health monitors, wearable communication devices, and other application that require lightweight, deformable format. [1]

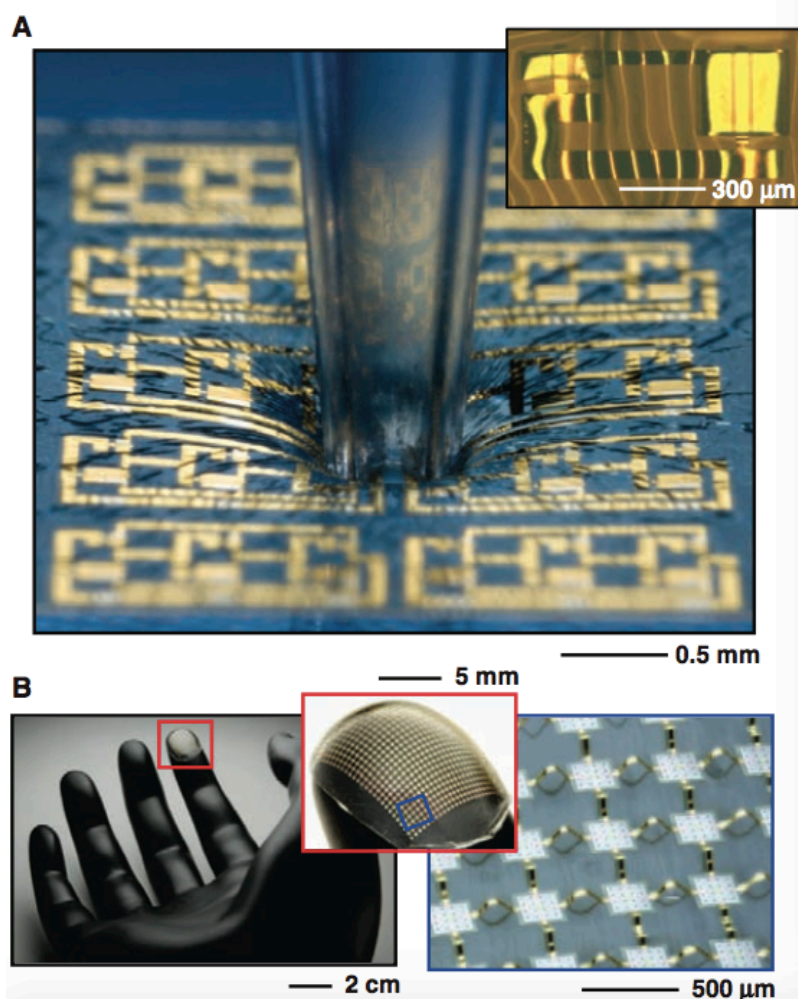


*Fig. 1.1. Examples of stretchable electronics. (A) Stretchable silicon circuit in a wavy geometry, compressed in its center by a glass capillary tube (main) and wavy logic gate built with two transistors (top right inset). (B) Stretchable silicon circuit with a mesh design, wrapped onto a model of a fingertip, shown at low (left), moderate (center) and high (right) magnification. The red (left) and blue (center) boxes indicate the regions of magnified views in the center and right, respectively. The image on the right was collected with an automated camera system that combines images at different focal depths to achieve a large depth of field. [1]*

The early study of this deformable electrical circuits [11] began with polymer transistors formed on bendable plastic sheets around 20 years ago. A lot of profound success followed, with contribution of advance printing and patterning techniques, devices with hundreds of active components are nearing commercial reality [12,13]. The deepened technology involves the development of new electronic materials that can flex, such as organic semiconductors or films of carbon nanotubes [14,15], new material conductors that can stretch, such as composite elastomer [16,17], or deformable circuits made-up of conventional conductors, such as Copper (Cu), Gold (Au) and Aluminum (Al), shaped on the basis of structural mechanic arguments so as to exhibit an enhanced effective compliance [13]. Two important parameters of the structure are well-studied in order to construct a stretchable structure, i.e. thickness and geometric configuration. [18]

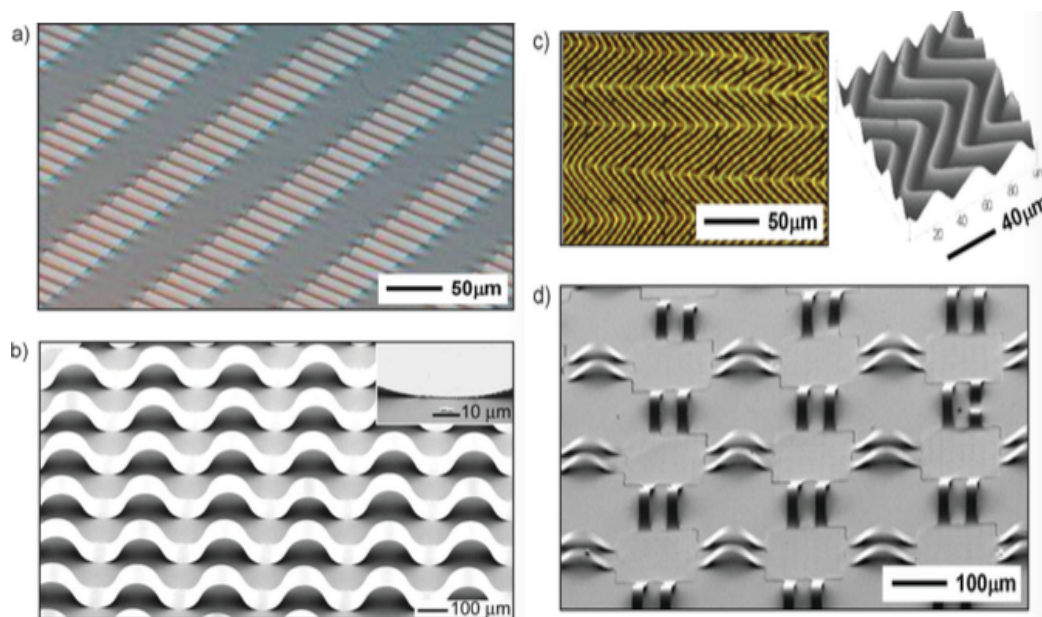


*Figure 1.2. Scanning electron microscopy (SEM) and optical microscopy images of inorganic structures in controlled buckling geometries on elastomeric substrates. a) SEM image of an array of silicon nanoribbons in wavy configurations on PDMS. b) SEM image of an array of gallium arsenide nanoribbons in buckled shapes where bonding to the PDMS substrate occurs only at the positions of the troughs. c) Optical microscopy (left) and atomic force microscopy images (right) of a wavy, silicon nanomembrane bonded to a PDMS substrate. d) SEM image of a silicon nanomembrane in a buckled, mesh layout on PDMS. Bonding is localized to the regions of the square islands. [19]*

Any material in sufficiently thin form is flexible, by the virtue that bending strains decline linearly along with thickness. This principle holds irrespective of the material stiffness. For example, a silicon wafer is known as brittle and rigid, but once it is fabricated in thin-film configuration with thickness values approaching the sub-micron range (e.g., nanoscale ribbons, wires or membranes), it becomes flexible. *Kim.D.H et al.* [10] has successfully achieved only 0.0005% peak strains to radii of curvature of 1cm, by making silicon as ribbons with thicknesses of 100nm. This peak strain is far below the fracture limits of silicon (~1%).

The mechanical performance can be further improved by constructing such structures in stretchable configurations. Commonly used stretchable configurations are:

- one dimensional ‘wavy’ ribbon mounted onto an elastomeric substrate (Fig.1.2.a)
- one dimensional buckled ribbon bonded to substrate only at positions of the troughs (Fig.1.2.b)
- two dimensional ‘wavy’ membrane (Fig.1.2.c)
- two dimensional buckled mesh. (Fig.1.2.d).

Other strategies, which do not involve out-of-plane motion, are also considered to be reasonable to construct stretchable inorganic structures. Coiled-spring is the first to be introduced (Fig.1.3.a). It obtains certain degree of stretchability if the coiled spirals are uncurled. Another planar strategy is to use leaf-arm springs (Fig.1.3.b). Stretchability is realized by pivoting motion mode. S-shaped (i.e., serpentine) structures are also exploited (Fig.1.3.c), in which bending at the corners accommodate applied strain.

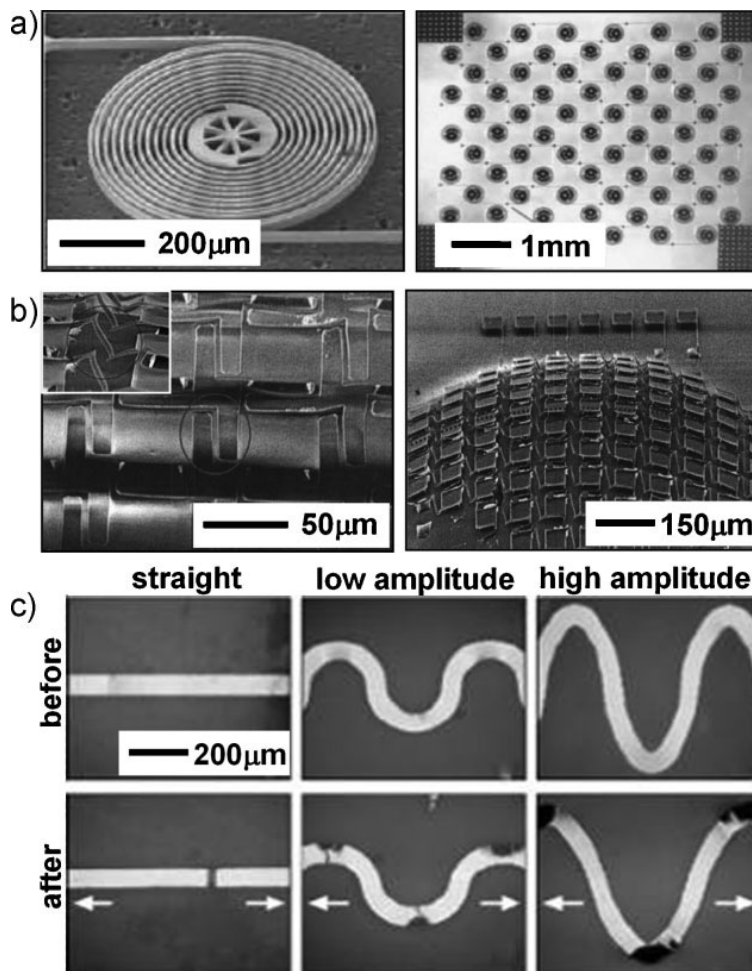


Figure 1.3. a) SEM image of an silicon structure etched into the shape of a spiral surrounding a central hub (left) and optical image of expanded, interconnected array of such structures (right). b) SEM image of silicon island interconnected with straight, leaf-spring type interconnects on an elastomeric film before (right) and after (right inset) stretching, and view of the array after expansion into a dome shape by applying pressure from the back side. c) Optical images of straight and serpentine metal lines (low- and high-amplitude structures) on an elastomeric substrate. The sequence of images on top shows the as-fabricated structures. The sequence of images on the bottom shows the same structures after application of tensile strain in the direction indicated by the arrows. The discolored regions correspond to deformations at locations of peak strain. [19]

## 1.2 Material choice for stretchable electronics

Stretchable electronics require integration of microelectronics onto deformable substrates. This involves material choice for both the deformable substrate and the patterned metal layer on top.

### **1.2.1 PDMS as Substrate**

For the sake of deformability, most of the substrate materials chosen by researchers in the field of stretchable electronics are polymers. The mostly used ones are: Polydimethylsiloxane (PDMS), Polyimide (PI) and Polyethylene terephthalate (PET). In this study, PDMS is chosen to be the stretchable substrate. PDMS is a silicone elastomer with desirable properties: in chemical and biomedical aspects, PDMS is inert and non toxic, stable under wide temperature range, easy to prepare, handle and modify [20]. Also, PDMS is compatible with microelectronic clean room equipment after proper preparation. These features allow applications under environment as complex as inner human body, and feasibility under microfabrication using chemicals. As concerns mechanical aspects, provided proper fabrication PDMS shows isotropic and homogeneous properties, which are important to accommodate exceeding strain from conductive layer on top. Extensive characterization of PDMS as a biocompatible material was presented by Mata and co-workers [20]. According to the results, chemical immersion does not show major changes in PDMS surface hydrophilicity, which indicates compatibility under microfabrication. Sterilization does not affect PDMS surface micro-textures, element concentration or hydrophilicity which proves feasibility of PDMS in biomedical application. Immersion in tissue culture media induced presence of nitrogen and an increase of O/Si ratio, which is likely due to ingredients presented on components such as amino acids and proteins. These components are rich in N and O, which deposit on the PDMS surface exposure to culture media. Additional care may be required in some specific biomedical application.



### **1.2.2 Gold on PDMS**

Gold is one of the most ductile metal with high electrical conductivity (44.2 S/m), and also biocompatible.

It has been shown that gold films on PDMS membranes can be stretched far beyond strain limit of gold film alone (up to 22% [3]), while still remain electrically conducting. The reason for the increase performance is that the electrical failure of a thin metal film is mainly due to mechanical fracture, and if the film is strongly bonded to a substrate compliant enough, the ductile failure is suppressed or delayed due to strain delocalization ensured by the polymeric substrate [21].

According to the study of stretchability of thin metal films on elastomer substrate [14], as a freestanding thin film, gold film rupture at around 1% strain. The value is smaller than that of corresponding bulk metals. The reason for this may be the fact that although a gold thin film is inherently ductile, the deformation is very localized and the film does not harden beyond modest strain. For a freestanding metal film, rupture is induced by a single neck. Once a neck is formed, further deformation of the film will take place only around this region. The film is thin, thus shows a small thickness-to-length ratio, which indicates that elongation at the single neck contributes very little to the overall rupture strain. Lacour et al. [21] proved that with larger rupture strains can be achieved by bonding the metal film to an elastomer substrate well and firm. They attempted and succeeded in obtaining additional stretchability of a few tenths of a percent by inducing a surface wave, i.e. random wrinkles, in thin gold film.

However, reliable deposition of metal upon elastomers is a challenging task. The mismatch in thermal expansion coefficient of Au and PDMS makes rise significant residual stresses as the system is fabricated in the temperature range of 100°C and approaches to room temperature [4]. Moreover, plasma-treatment of the polymer surface to enhance subsequent metal/polymer adhesion can cause a significant embrittlement of the polymeric material across a few tenths of nanometers depth from the surface [5]. The combination of the aforementioned phenomena can trigger the onset of undesired cracks, which affect both the metal film and the embrittled layer of the polymer substrate at very limited strains, or even in the undeformed state.

The sample used in this study is Au thin film deposited on PDMS substrate. An overview of the sample surface is shown in Fig.1.4.

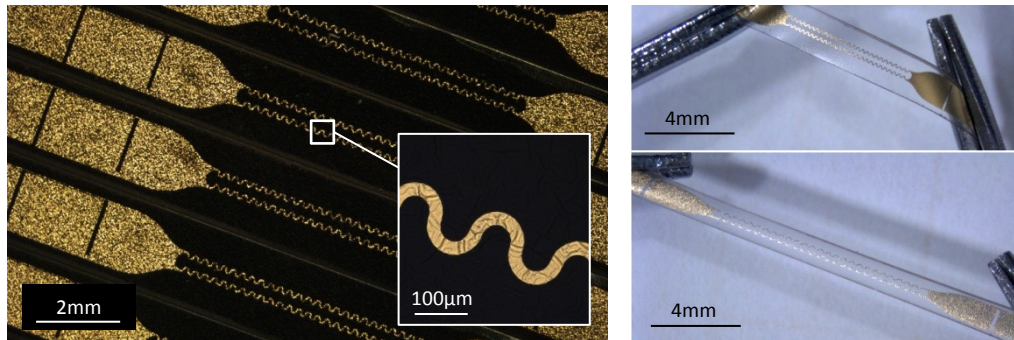


Figure 1.4. Au/PDMS samples with a detail of one of the meander geometries(right); Undeformed (right top) and stretched (right bottom) Au/PDMS sample.

One of our colleague had performed uniaxial stretch with in-situ SEM, and the result revealed extensive wrinkling and cracking of the system during stretch. The crack evolution of Au thin film on top corresponding to strain history is the main interest in this study.

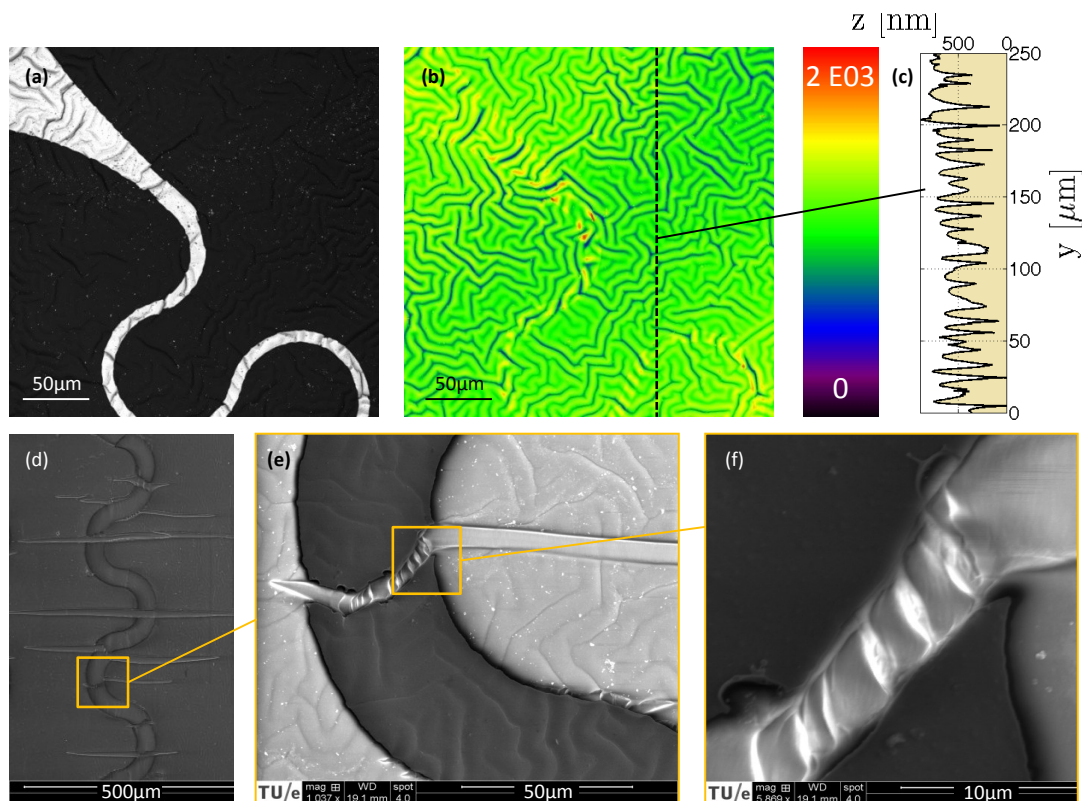


Figure 1.5. a) reflected intensity and (b) height map of a Au/PDMS sample. The dashed black line indicates where the (c) line profile of the wrinkled surface was measured; (d) SE micrograph showing extensive cracking on the PDMS surface upon 15% strain; (e) crack across the Au film and (f) detail of the compliant PDMS fibrils exposed below the embrittled surface.

## 1.3 Testing methods for thin film properties

There exist several other testing methods to obtain thin film properties. Uniaxial micro-tensile tests, nanoindentation and bulge testing are among the most popular examples. Bulge testing is the experimental technique pursued in this work and its principles are thoroughly described in Chapter 2. For the sake of completeness and comparison with the technique, in continue the uniaxial micro-tensile and nanoindentation techniques will also be briefly described.

### **1.3.1 Uniaxial micro tensile test**

Uniaxial tensile test can measure strain directly on the specimen with suitable extensometers. But for thin films with refined thickness, this technique requires special techniques and procedures for sample preparation, handling and loading. Comparing to the traditional uniaxial tensile test at the marco scale, the alignment and gripping system should be carefully devised, due to the fact that even limited drift from the nominal performance will induce large deviation in the micro scale experiment.

Two different kind of set up will be introduced in this section, both of which are mostly referred to by researchers in the field of thin films mechanics. The first one of was built up by Sharpe et al. [22], the second was by Ogawa et al. [23].

Sharpe et al. [15]: In this system, strain is measured with an interferometric strain/displacement gage (ISDG). Precise load measurement is enabled by an air bearing system to avoid friction and a periodically calibration is done to loading system. Both strain and load are measured and recorded to a computer on a real-time basis.

The ISDG is an optical technique to measure strain or displacement between two reflective gage markers on the specimen. *Two-slit interference* by Young served as optical principle of ISDG, but reflection is detected instead of transmission.

A pair of gold pads or lines are deposited on the specimen as marker to generate interference fringe from their slightly inclined edges.

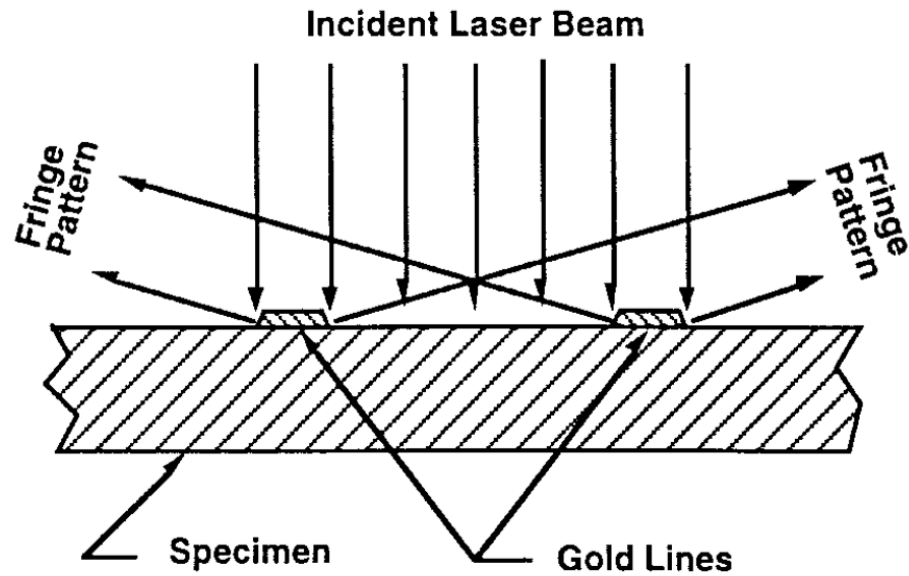


Figure 1.6. Schematics of the ISDG [22]

When both markers are illuminated with laser, a diffracted reflection interfere with each other, so the fringes are formed. While markers move relative to each other, the fringe patterns change and the motion can be detected so as to obtain relative displacement due to strain. Rigid-body motion will also cause the fringes to move, so it is necessary to average the movement of the two fringe patterns. The equation to obtain strain from fringe motion is:

$$\varepsilon = \frac{\lambda}{2d_0} \left( \frac{\Delta m_1}{\sin \alpha_1} + \frac{\Delta m_2}{\sin \alpha_2} \right) \dots \dots (Eq. 1.1)$$

Here  $\Delta m_1$  and  $\Delta m_2$  are the relative fringe shifts of patterns,  $d_0$  is the initial gage length between the indentations,  $\lambda$  is the wavelength of the laser, and  $\alpha_1$ ,  $\alpha_2$  are the angles between the incident laser beam and fringe patterns.

The fringe patterns can be converted into electrical signals by means of photodiodes.

Specimens used in this uniaxial micro tensile test is polysilicon and should be manufactured and handled *ad-hoc*. Fig 1.7. shows the specimen schematic. Noted that support strip is defined at top and bottom, and a rectangular area in the center is etched away so to free the specimen between two grip ends.

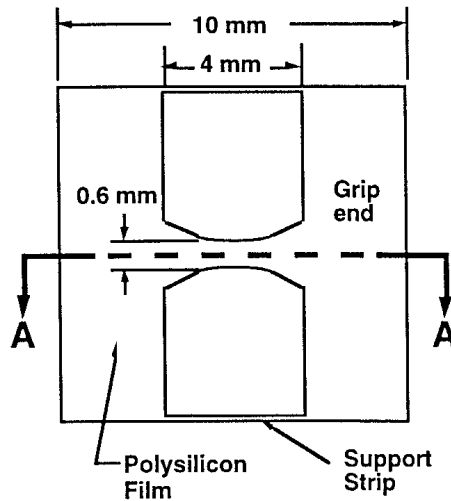


Figure 1.7. Schematics of a manufactured specimen [22]

Fig 1.8 shows a possible release handling of specimen process.

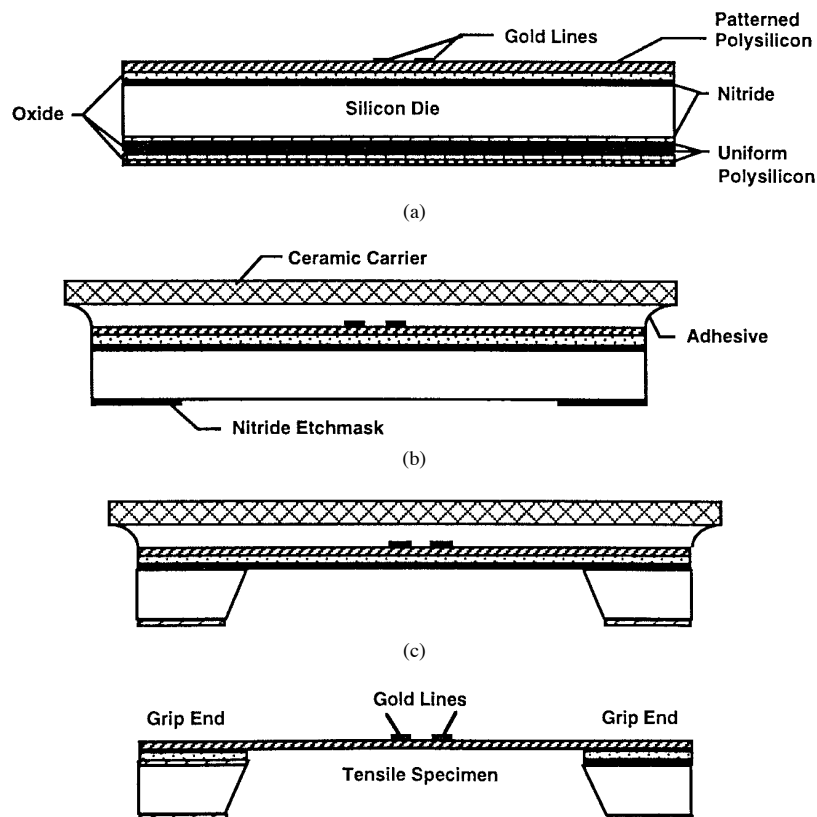


Figure 1.8. Steps to release the tensile specimen viewed in section A-A[22]

A ceramic carrier is mounted on the die using adhesive wax, which aims to protect the polysilicon specimen.

A schematic of the measurement system is given in Figure 1.9. The grip is fixed on one side and attached to a linear air bearing on the other. The linear air bearing, which is used to minimize the friction in loading system so as to gain accurate load measurement, connects to a load cell. Displacement or load is applied by the piezoelectric actuator which follows commands from computer, thus load is recorded simultaneously. The fringe motions are converted into strain. Combining two, the load/strain curve is obtained.

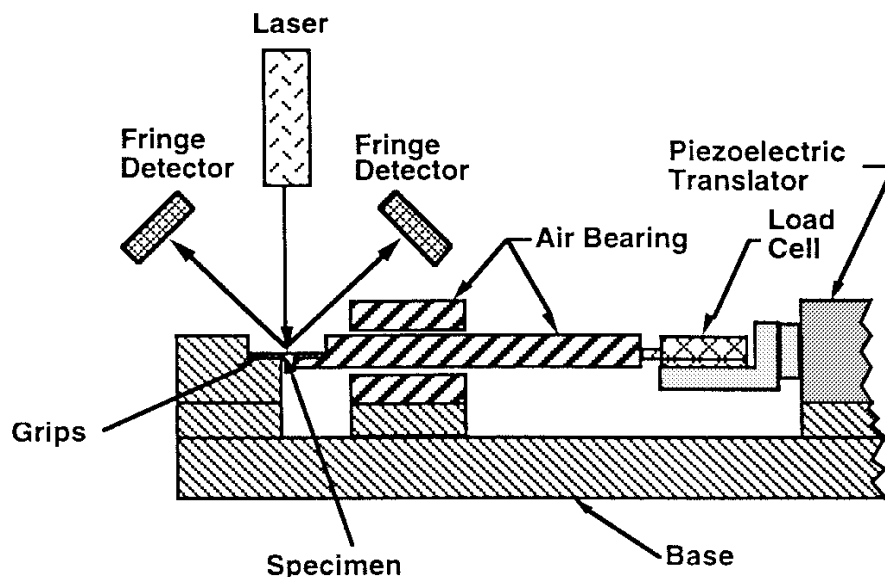


Figure 1.9. Schematic of the measurement system [22]

1) Ogawa et al. [23]:

The uniaxial tensile test set up by Ogawa et al. differs from the one presented by Sharpe et al. only with reference to the strain measurement technique. Following the similar procedure, marked specimens with identical shape are obtained.

The strain was determined by measuring the relative displacement of the marks, but instead of using laser interferometer, a double-field-of-view microscope is used, combining with two Charge Coupled Device (CCD) cameras and image synthesizer

and an image processor. This means that the strain is measured by processing the images.

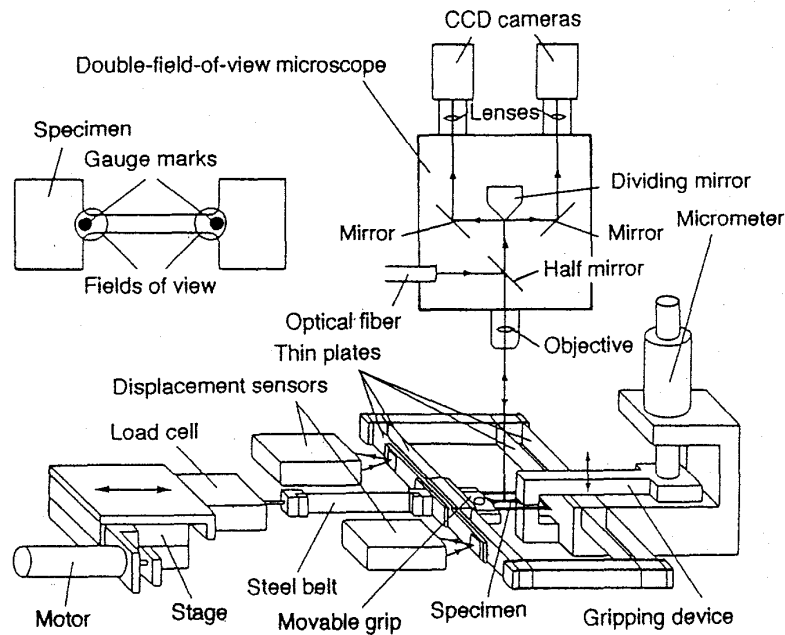


Figure 1.10. Schematic of the tensile test machine set up [23]

To mount the specimen on the machine and grip it, Ogawa and co-workers designed a different mechanism. The specimen is mounted on the movable grip and clamped with a screw and a plate, then it is better fixed by a micrometer.

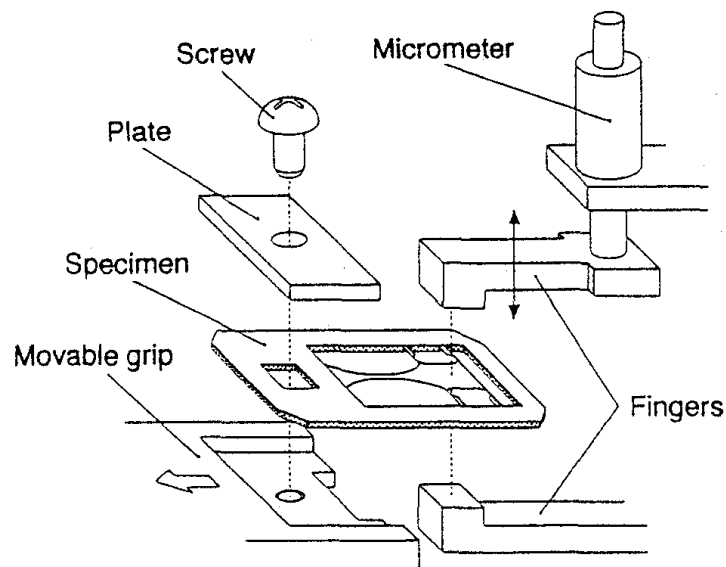


Figure 1.11. Schematic of the specimen mounting [23]

### 1.3.2 Nanoindentation [24] [25]

Nanoindentation is one of the most widely used test method to study mechanical properties of thin films. A sharp diamond (from now on referred to as *indenter*) is led against the surface of the specimen, which in this case consists in a thin film on a substrate. Depending on the specific indentation system, the force can be controlled and the corresponding displacement of the indenter is measured, or *vice versa*.

Nanoindentation technique can measure hardness, elastic properties and time-dependent deformation of thin films. It can also serve as an indenter to induce fracture of sub-micron scale, for the measurement of fracture toughness. Fig.1.10 shows the most commonly used tips and their indentation shape for nanoindentation techniques.

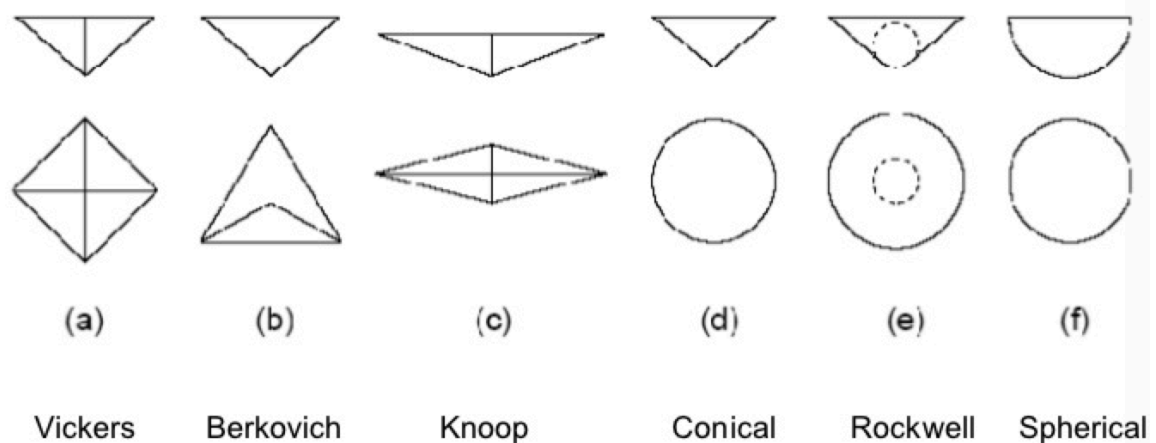


Figure 1.12. Schematics of most commonly used tips and corresponding indentation shape

A known stiffness indenter (usually diamond) with calibrated shape is pressed into the sample, the sample surface deforms both elastically and plastically, a conforming shape hardness impression is formed. While the indenter withdraws, only the elastic portion of deformation is recovered. Hence a load-displacement curve can be obtained and desired properties can be abstracted and calculated through the curve.

Fig.1.13 shows a schematic diagram of a nanoindenter. The load is applied and controlled by the current in the coil coupled with a permanent magnet. Indenter column is supported by a leaf springs, which are part of the capacitance device for measuring displacement.



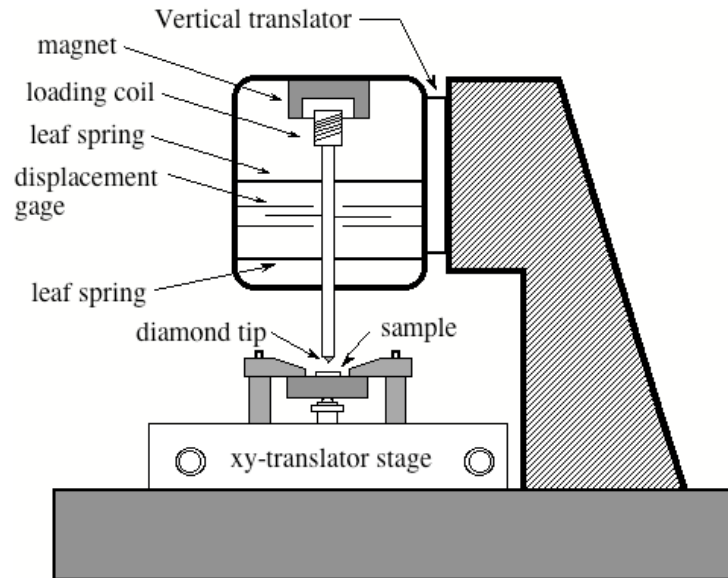


Figure 1.11. Schematics of most commonly used tips and corresponding indentation shape

Hardness is defined as the indentation load divided by projected contact area of indentation.

$$H = \frac{P_{max}}{A} \dots \dots (Eq. 1.2.)$$

Measurement of the projected contact area  $A$  from a load-displacement curve requires  $h_c$ , the contact depth. For an indenter with a known geometry, for example, an ideal Berkovich indenter,

$$A = 24.56h_c^2 \dots \dots (Eq. 1.3.)$$

The contact depth can be estimated from the load-displacement data:

$$h_c = h_{max} - \varepsilon \frac{P_{max}}{S} \dots \dots (Eq. 1.4.)$$

Here  $\varepsilon$  is a constant that depends on the indenter geometry; for a Berkovich indenter, it equals 0.75.

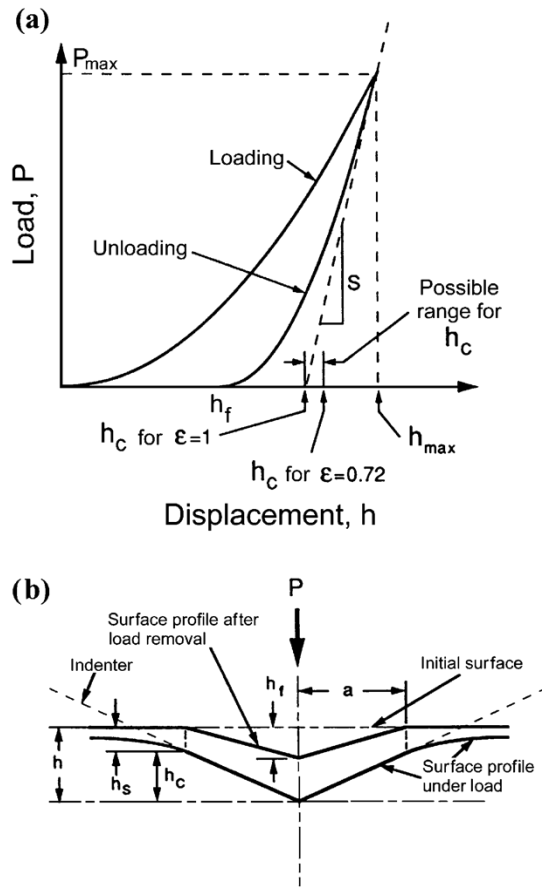


Figure 1.12. (a) A typical load-displacement curve; (b) the deformation pattern of an elastic-plastic sample during and after indentation.

The elastic modulus of the indented sample can be obtained by the initial unloading contact stiffness, i.e., the slope of the beginning part of the unloading curve.

$$S = \frac{dP}{dh} \dots \dots (Eq. 1.5.)$$

$$S = 2\beta \sqrt{\frac{A}{\pi}} E_r \dots \dots (Eq. 1.6.)$$

$$E_r = \frac{1 - \nu^2}{E} + \frac{1 - \nu_i^2}{E_i} \dots \dots (Eq. 1.7.)$$

Here  $\beta$  is a constant that depends on geometry of indenter, for Berkovich it is 1.034, and  $E_r$  is the reduced elastic modulus, due to the fact that both the sample and the indenter deform.  $E$  and  $\nu$  are the elastic modulus and Poisson's ratio of the sample, while  $E_i$  and  $\nu_i$  are those of indenter (for diamond,  $E_i = 1141 \text{ GPa}$  and  $\nu_i = 0.07$ ).

It should be noted that the elastic properties from previous equation hold for the sample thin film only when the film thickness is much greater than the indentation depth, in order to reasonably assume that the mechanical response is not affected by the substrate properties. While for metal thin films on hard substrates, a ratio of 10 times between film thickness and indentation depth is generally accepted [26], when metal films are deposited on compliant substrate, the contribution of the latter to the overall deformation cannot generally be neglected, therefore the aforementioned analytical treatment wouldn't hold for indentation on material systems for stretchable electronics applications

In this section, two testing method for thin metal films, which are alternative to bulge test, were introduced. They both have their limitations.

- As concerns uniaxial micro-tensile tests, experimental results can be greatly affected by alignment and gripping of the setup. Also, non-trivial sample fabrication and handling required and the uniaxial strain state can only be achieved, unless the device is upgraded by multiplying its degrees of freedom (therefore the number of driving systems, and consequently the final cost of the device);
- For nanoindentation, when thin metal films on compliant polymers are considered, the suitability of analytical treatments for the interpretation of experimental results falls due the high deformability of the substrate. Furthermore, nanoindentation inherently induces a very localized strain state. While this feature makes it a very suitable technique for non-destructive mechanical characterization of materials, it wouldn't be possible to replicate the stress/strain field of common stretchable electronic components in service, which typically involves a much bigger characteristic length scale as compared to that of an indentation area. Last, small scale mechanics study significantly benefit from in-situ observations (e.g., by means of optical or scanning microscopy) to gain insight on the evolution of deformation and/or failure mechanisms. As mentioned, the design of common nanoindenters is non-trivial

and generally results in bulky setups, which require an *ad-hoc* installation to operate in combination with optical or scanning microscopes.

Following these arguments, an alternative mechanical testing technique was considered in this work, namely, the bulge testing technique.

## 2 Bulge Testing Technique: Theoretical Principles [24]

This chapter is about the bulge test method used in this project. After brief history of this specific technique, the theory of bulge test will be presented. Bulge equations for different sample shape will be presented. Later, the general setup for bulge test will be describe, as guidance to the manufacture and mounting in our project.

### 2.1 Bulge test introduction

Bulge test has its unique advantages of precise sample fabrication and minimal sample handling. It is a non-destructive test method, it usually features a relatively simple and portable design (compared to nanoindentation), and can reproduce more than one kind of stress/strain state in a very cost-effective manner (compared to uniaxial tensile stress test), namely by tuning the shape of the so called *bulge window*, which defines the shape of the specimen itself.

Bulge test determines mechanical properties of free standing thin films by applying pressure on one side and measuring the corresponding deflection. Its theory was first developed in 1915 by Hencky. [27] Beams [28] then introduced this idea into measurement of material properties. He began with very simple pressure deflection relationship, which lack further theoretical backup. Later, Tsakalakos [29] developed the theory for circular membranes. Small [30] took into consideration also the intrinsic stress of the film and initial height of the membrane. Vlassak and Pratt [31],[32] developed the theory for square membrane, but it is still too complex and thus lack of further usage. Likewise, Tabata and Vlassak [33],[31] developed the theory for rectangular membranes, and this improvement supports a broadened variety of application.

## 2.2 Bulge equations

It is worth mentioning that, from now on, the term *sample* or *thin-film* will refer to the full material system considered in later chapters of this study, namely Au film on PDMS substrates. The reason is that, considering the aspect ratio of the samples (and that of metal/polymer systems for general application in the stretchable electronics field) the whole materials system mechanically behaves as a composite thin film. Furthermore, when the thickness of the metal layer is much less than that of the polymeric substrate, the overall mechanical behavior can be assumed to be governed by the polymeric substrate. For the sake of clarity, it is worth stating that the bulge testing technique will not be presented as a mean to characterize the metal film properties separately with respect to the substrate mechanics. Conversely, the bulge test technique will be mainly exploited to investigate the mechanics of the polymeric substrate and infer the resulting strain experienced both by the polymer surface and the bonded metal film.

In continue, the bulge equation will be presented in the traditional framework of linear elasticity. The central deflection ( $h$ ) is directly related to the strain experienced by the sample, while the applied pressure ( $p$ ) is related to stress. Thus, mechanical properties of thin film material can be extracted by measuring the pressure/ deflection relationship and knowing the so called *window size and shape*, which refers to the geometrical features of the cavity whose boundaries define the sample dimension and shape. This cavity will be form now on refreed to as *bulge window*.

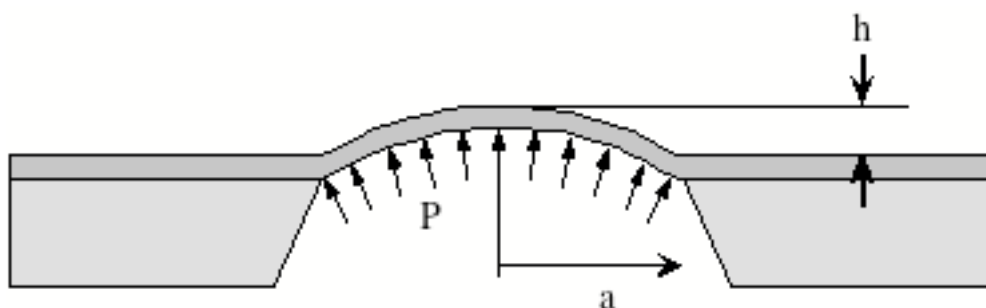
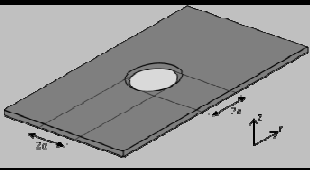
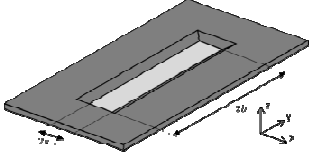
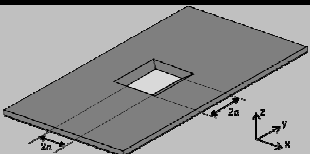


Fig.2.1. Main parameters in bulge test method[24]

The bulge window is extremely important because its shape defines the strain state experienced by the sample, which means that by proper tuning of the bulge window

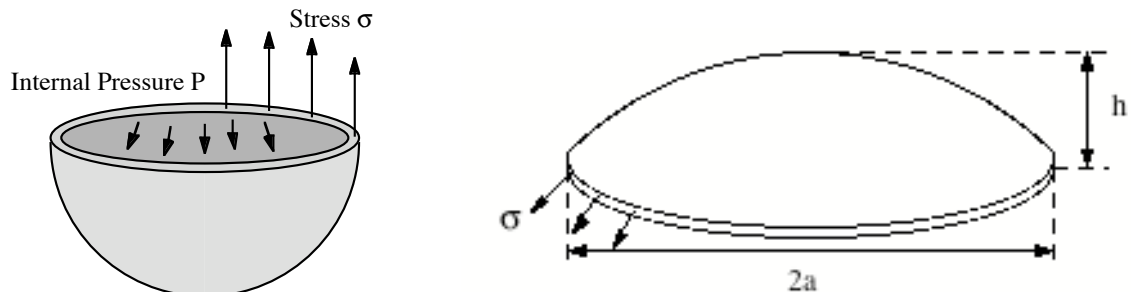
shape, different deformation states can be studied. The table below shows summary of different geometries used for bulge test. Later in this chapter, the path to obtain bulge equations will be illustrated.

Table 2.1. Summary of the different geometries used for bulge test [34]

Geometry	Stress/Strain state of the center of the membrane	Stress and Strain	Bulge Equation
			$p = C_1 \sigma_0 t \frac{\delta}{a^2} + C_2 \frac{E}{1-\nu} t \frac{\delta^3}{a^4}$
	Equi-biaxial stress $\sigma_{tan} = B(\varepsilon_{tan} - \varepsilon_0) + \sigma_0$	$\sigma_{tan} = \frac{a^2 p}{4 \delta t}$ $\varepsilon_{tan} = \frac{2 \delta^2}{3 a^2} + \varepsilon_0$	$C_1 = 4$ $C_2 = \frac{8}{3}$
	Plane strain $\sigma_{tan} = M(\varepsilon_{tan} - \varepsilon_0) + \sigma_0$	$\sigma_{tan} = \frac{a^2 p}{2 \delta t}$ $\varepsilon_{tan} = \frac{2 \delta^2}{3 a^2} + \varepsilon_0$	$C_1 = \frac{2}{4}$ $C_2 = \frac{1}{3(1+\nu)}$
	Transition state	No straight forward analytical expression	$C_1 = 3.939$ $C_2 = \frac{1}{(0.792 + 0.085\nu)^3}$

## 2.3 Circular window model of the bulge test

A pressurized thin-film clamped by circular window can be modeled as a section of a thin-walled spherical cap.



*Fig.2.2. Schematic sketch of a bulged film in spherical shape*

Wall thickness is  $t$ , and radius is  $R$  (not indicated in the picture). The stress in the thin wall is obtained by force equilibrium due to stress and pressure.

$$p \cdot \pi R^2 = \sigma \cdot 2\pi R t \dots \dots (Eq. 2.1.)$$

$$\sigma = \frac{pR}{2t} \dots \dots (Eq. 2.2.)$$

Note that  $2\pi R t$  is actually the cross section area of thin wall. Here, in the spherical bulge model, the stress is in-plane and equi-biaxial, ( $\sigma_{xx} = \sigma_{yy}$ ). We also call it as plane stress condition. These equations indicate the relationship between applied pressure, radius of curvature, and stress in the bulged thin film.

A bulged film in reality (right of Fig.2.2) is like a slice of the spherical vessel on the left. Letter “a” indicates window radius.

In general bulge test models, one considers only relatively small deflections ( $h \ll a$ ). From pure geometry, one can write the relationship between deflection height, window size and membrane curvature radius.



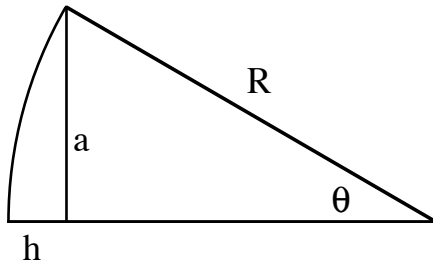


Fig.2.3. Schematic sketch of cross section of thin film and its geometry

The relation can be written as:

$$R^2 = (R - h)^2 + a^2 = R^2 - 2Rh + h^2 + a^2 \approx R^2 - 2Rh + a^2 \dots \dots (Eq. 2.3.)$$

Noted that  $h^2$  is relatively small, as mentioned before, thus  $h^2$  is neglected. So Eq.2.3 can be rearranged as:

$$R = \frac{a^2}{2h} \dots \dots (Eq. 2.4)$$

By making a substitution to Eq.2.2, one can get the stress expression:

$$\sigma = \frac{pR}{2t} = \frac{pa^2}{4th} \dots \dots (Eq. 2.5.)$$

Then the strain can be computed, in the view of its correlation with the stress by means of the material properties. The relationship between deflection and film strain can be obtained by pure geometry:

$$\varepsilon = \frac{R\theta - a}{a} = \frac{\theta - \left(\frac{a}{R}\right)}{\left(\frac{a}{R}\right)} \dots \dots (Eq. 2.6.)$$

Using Taylor Expansion, the following expression is obtained:

$$\theta = \arcsin\left(\frac{a}{R}\right) = \left(\frac{a}{R}\right) + \frac{\left(\frac{a}{R}\right)^3}{6} + \dots \dots \dots (Eq. 2.7.)$$

By terminating the expansion at the third order, the strain can be expressed as:

$$\varepsilon = \frac{a^2}{6R^2} = \frac{2h^2}{3a^2} \dots \dots (Eq. 2.8.)$$

For linear biaxial elastic strain,

$$\sigma = B\varepsilon = \frac{2Bh^2}{3a^2} \dots \dots (Eq. 2.9.)$$

Where  $B = E/(1 - \nu)$  is the reduced modulus in equi-biaxial conditions.

Recalling the relationship of stress and pressure in Eq.2.5., and one can get get:

$$\sigma = \frac{pa^2}{4th} = \frac{2Bh^2}{3a^2} \dots \dots (Eq. 2.10.)$$

By rearranging the equation, the desired deflection-pressure relationship is obtained:

$$p = \frac{8Bth^3}{3a^4} = \frac{8h^3}{3a^4} \frac{Et}{1 - \nu} \dots \dots (Eq. 2.11.)$$

This is the bulge equation for a bulge window of spherical shape.

If the residual stress of the membrane is also considered, one can simply rewrite the stress strain relationship, including also residual stress in material behavior.

$$\sigma = B\varepsilon + \sigma_0 = \frac{B2h^2}{3a^2} + \sigma_0 = \frac{pa^2}{4th} \dots \dots (Eq. 2.12.)$$

So the bulge equation becomes:

$$p = \frac{8Bt}{3a^4} h^3 + \frac{4\sigma_0 th}{a^2} \dots \dots (Eq. 2.13.)$$

But in this study, residual stress was not investigated. Therefore, the residual stress term is presented here as a corollary of the theoretical background on the traditional treatment of bulge testing.

## 2.4 Rectangular window model for bulge test

Rectangular window is in fact the mostly used shape for bulge test device, due to its easier control over shape. Rectangular constraints also induce a biaxial behavior, but it is no longer equi-biaxial. Instead, in this model, the membrane is in plane-strain condition.

Rectangular windows for bulge test should feature an aspect ratio ( $b/a$ , see Figure 2.4) larger than four, in order to be immune from shape deviation effect [33]. By looking at the strains along a-direction and b-direction, it can be stated that, as long as aspect ratio is large enough ( $b/a > 4$ ), strain in a-direction is relatively large, while strain in b-direction is very small and thus can be neglected. Furthermore, away from the ends of the rectangle, the film is assumed to have a uniform radius of curvature.

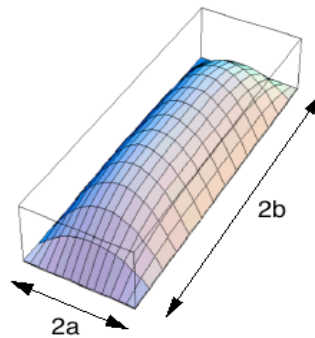


Fig.2.4. Schematic sketch of rectangular window shaped membrane

When the strain in one direction is almost zero, plane strain conditions apply. One can write the stress-strain relationships in this condition: ( $x$  is the Cartesian coordinate in the direction of  $a$ , while  $y$  is the Cartesian coordinate aligned with the dimension  $b$ .)

$$\begin{aligned}\varepsilon_{xx} &= \frac{1}{E} (\sigma_{xx} - \nu\sigma_{yy}) \\ \varepsilon_{yy} &= \frac{1}{E} (\sigma_{yy} - \nu\sigma_{xx}) = 0 \dots \dots (Eq. 2.14.)\end{aligned}$$

which leads to

$$\begin{aligned}\sigma_{yy} &= \nu\sigma_{xx} \\ \varepsilon_{xx} &= \frac{\sigma_{xx}(1 - \nu^2)}{E} \dots \dots (Eq. 2.15.)\end{aligned}$$

Like in the previous plane stress condition,  $(1 - \nu^2)/E$  can be considered as the reduced modulus in the plane strain case.

In the spherical model, the thin film is considered as thin-walled spherical cap, while in the rectangular window, the deformed membrane can be modeled as a cylindrical thin wall (see Figure 2.5).

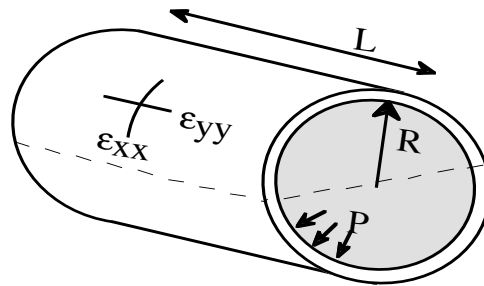


Fig.2.5. Schematic sketch of cylindrical thin-walled model

The thickness of the wall is noted as “t”. Writing the force equilibrium equation for half of the cylinder, the following expression is obtained

$$2R \cdot L \cdot p = 2t \cdot L \cdot \sigma_{xx} \dots \dots (Eq. 2.16.)$$

$$\text{Thus } \sigma_{xx} = Rp/t \dots \dots (Eq. 2.17.)$$

Once the relationship between stress and pressure is obtained, the bulge equation to describe long rectangular windows can be derived.

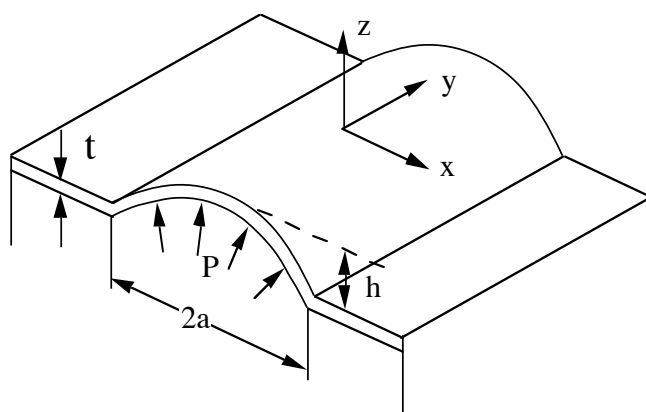


Fig.3.6. Schematic sketch of model of bulged rectangular membrane

Recalling the constitutive relationship in plane strain conditions (Eq.2.15.) and combining with the stress-pressure relationship (Eq.2.17.), the bulge equation for rectangular window shapes can be obtained, once noted that the same geometric arguments between strain, curvature, deflection and window size described for the circular case also apply for a cylindrical profile, Eq.2.4 and Eq.2.8. can be also applied.

So one can obtain bulge equation for rectangular membrane model:

$$p = \frac{3 h^3}{4 a^4} \frac{E t}{1 - \nu^2} \dots \dots (Eq. 2.18.)$$

When the effect of residual stresses is introduced, the following expression can be obtained

$$\sigma_{xx} = \frac{2 h^2}{3 a^2} \cdot \frac{E}{1 - \nu^2} + \sigma_0 \dots \dots (Eq. 2.19.)$$

$$p = \frac{2 h t \sigma_0}{a^2} + \frac{4 h^3}{3 a^4} \frac{E t}{1 - \nu^2} \dots \dots (Eq. 2.20.)$$

## 2.5 Square Windows

The last shape of window to mention about is square ones. This choice is less popular, since it requires a more complex analytical treatment. Nevertheless, as a completion of theoretical background, it is induced in this chapter.

In square windows, deflection is not defined to a single direction. It varies in two dimensions, which complicates the analytical treatment to obtain the pressure/deflection relation. Approximate solutions can be obtained using energy-minimization method. In continue, the outline of procedure is listed.

1. Assume there exist a certain form of displacement function, with unknown coefficients ( $A, w_0, w_1$ ) to be determined. They are equivalent to the first two terms of a Taylor series expansion. Quantities of displacements in the ( $x, y, z$ ) direction are ( $u, v, w$ ) respectively.

$$u = \frac{A}{a^4} x(a^2 - x^2)(a^2 - y^2)$$

$$v = \frac{A}{a^4} y(a^2 - x^2)(a^2 - y^2)$$

$$w = \frac{w_0}{a^4} \left( 1 + \frac{w_1}{a^2} (x^2 + y^2) \right) (a^2 - x^2)(a^2 - y^2) \dots \dots (Eq. 2.21.)$$

2. Strains can be derived from the displacement functions:

$$\varepsilon_{xx} = \frac{\partial u}{\partial x} + \frac{1}{2} \left( \frac{\partial w}{\partial x} \right)^2$$

$$\varepsilon_{yy} = \frac{\partial v}{\partial y} + \frac{1}{2} \left( \frac{\partial w}{\partial y} \right)^2$$

$$\varepsilon_{xy} = \frac{\partial u}{\partial y} + \frac{\partial v}{\partial x} + \frac{\partial w}{\partial x} \frac{\partial w}{\partial y} \dots \dots (Eq. 2.22.)$$

3. According to the principle of energy balance, the total potential energy of the membrane is equal to the strain energy minus the work done by the applied pressure:

$$V = \frac{Et}{2(1-\nu^2)} \iint (\varepsilon_{xx}^2 + \varepsilon_{yy}^2 + 2\nu\varepsilon_x\varepsilon_y + \frac{1}{2}(1-\nu^2)\varepsilon_{xy}) dx dy - \iint p w dx dy \dots \dots (Eq. 2.23.)$$

4. Minimize the total potential energy with respect to each of the coefficients in order to solve the unknown coefficients:

$$\frac{\partial V}{\partial A} = 0, \quad \frac{\partial V}{\partial w_0} = 0, \quad \frac{\partial V}{\partial w_1} = 0$$

5. This provides a set of three equations with three unknowns, which can be solved numerically leading to the pressure/deflection relation for square bulge windows

$$p = \frac{1}{(0.792 + 0.085\nu)^3} \frac{Et}{1-\nu} \frac{h^3}{a^4} + \frac{3.393\sigma_0 th}{a^2} \dots \dots (Eq. 2.24.)$$

## 2.6 Conclusion and discussion

### Comparison and discussion of result

By comparing the bulge equation obtained for the spherical model, the rectangular model and the square model, the main differences rely on:

- 1) The numerical coefficients before two terms.
- 2) The reduced modulus is different for rectangular model.

Thus, combining experimental data from rectangular windows, and either square or round windows, and neglecting the effect of residual stress, two equations for two unknowns are obtained, the unknowns being  $E$  and  $\nu$ . Thus Young's Modulus and Poisson Ratio of a linear elastic material can be obtained by combining experimental results corresponding to different window shapes.

### Possible sources of error in bulge test

In continue, the most common sources of error within a bulge test are listed.

- 1) Mounting the film

The delicate mounting would be discussed in future chapter. But one should notice that experiment condition and the proficiency of performer is one of the crucial aspect to ensure a better result. While mounting the film, one should try his best to ensure that the film is well-supported, free-standing and not wrinkled. Any wrinkling can result in significant errors.

- 2) Non-flat Films

The initial condition of the film is another major problem that one may face while performing a bulge test. Especially when using the laser interferometry to measure deflection, one should ensure that the film is flat within the resolution



of the equipment. Otherwise, one should modify the equation by inducing an “initial height”,  $h_i$ :

$$p = \frac{c_1 \sigma_0 t}{a^2} (h - h_i) + \frac{c_2 E t}{(1 - \nu) a^4 (h - h_i)^3} \dots \dots (Eq. 2.25.)$$

### 3) Residual Stress

From the previous equations, it is clear that residual stresses take significantly affect the reliability of experimental results. Residual stresses are induced mainly during the sample preparation. Therefore, to minimization of residual stresses usually rely on the optimization of the sample fabrication procedure.

## 3 Development of the Hyperelastic Bulge Equation

A pressure-deflection relationship is required in order to achieve a known strain loading in the membrane by controlling the pressure value and the window size. In this way, the crack evolution history of our Au/PDMS samples can be studied as a function of the strain history rather than the pressure value, which for a given material, would lead to a different strain state depending on the window size and shape.

Nevertheless, due to the elastomeric nature of the PDMS substrate, the traditional bulge equation would not be suitable to model the pressure/deflection response of the Au/PDMS samples (which, as mentioned, is governed by the PDMS response). In continue, the bulge equation is reviewed in the framework of incompressible hyperelasticity. Specifically, the pressure/deflection relation is derived analytically for a general hyperelastic strain energy potential. Then, the potential use of the hyperelastic bulge equation is shown by computing pressure/deflection curves by means of a MATLAB script.

Modeling assumptions read as follows

- i) The extremely thin gold layer on top does not affect the overall mechanical response of the PDMS membrane
- ii) PDMS behaves as an incompressible hyperelastic material
- iii) The sample does not experience significant residual stresses

In what follows, circular and rectangular bulge window shapes will only be considered.

### 3.1 Basic of hyperelasticity

Isotropic, continuum materials for which the constitutive behavior is merely a function of current state of deformation are known as elastic material, while for hyperelastic materials, the work done by the stresses during deformation process is dependent on the initial state and final configuration [33].

Certain operations on the strain tensor give the same result without regard to which orthonormal coordinate system is used to represent the components of strain. The results of these operations are called strain invariants. The most commonly used strain invariants can be written in terms of components as following:

$$\begin{aligned}
 I_1 &= \varepsilon_{11} + \varepsilon_{22} + \varepsilon_{33} \\
 I_2 &= \varepsilon_{12}^2 + \varepsilon_{23}^2 + \varepsilon_{31}^2 - \varepsilon_{11}\varepsilon_{22} - \varepsilon_{22}\varepsilon_{33} - \varepsilon_{33}\varepsilon_{11} \\
 I_3 &= \varepsilon_{11}(\varepsilon_{22}\varepsilon_{33} - \varepsilon_{23}^2) + \varepsilon_{12}(\varepsilon_{12}\varepsilon_{33} - \varepsilon_{23}\varepsilon_{31}) + \varepsilon_{13}(\varepsilon_{12}\varepsilon_{23} - \varepsilon_{22}\varepsilon_{31}) \dots \dots (Eq. 3.1.)
 \end{aligned}$$

One can describe the constitutive behavior of a hyperelastic material using a strain energy function  $\Psi$ . Most of the strain energy functions are a function of the strain invariants  $\Psi=\Psi(I_1, I_2, I_3)$ , or sometimes, of stretches  $\Psi=\Psi(\lambda_1, \lambda_2, \lambda_3)$ . Noted that the Cartesian coordinates are used in the modelling, and the direction 1 is the direction along the window size, which are mostly concerned. By definition, the stretch is the ratio of current length and the initial one:  $\lambda = \frac{L_{current}}{L_{initial}}$ .

For hyperelastic material, stresses are derived from the strain energy function  $\Psi$ . And for incompressible hyperelastic materials, the relations can be written as:

$$\begin{aligned}
 \sigma_1 &= \frac{\lambda_1}{J} \frac{\partial \Psi}{\partial \lambda_1} - p \\
 \sigma_2 &= \frac{\lambda_2}{J} \frac{\partial \Psi}{\partial \lambda_2} - p \\
 \sigma_3 &= \frac{\lambda_3}{J} \frac{\partial \Psi}{\partial \lambda_3} - p \dots \dots (Eq. 3.2.)
 \end{aligned}$$

Here,  $J = \lambda_1 \lambda_2 \lambda_3$ , and is equal to 1 due to the hypothesis of material incompressibility.  $p$  is the hydrostatic pressure induced by incompressibility.

$\sigma_3$  is the Cauchy stress component along the direction of membrane thickness. the boundary condition at the outer surface of the membrane, which is unloaded, reads as  $\sigma_3 = 0$ . Since the sample features a very small thickness, the stress component along the radial direction is assumed to provide a negligible contribution to equilibrium, therefore a very common approximation corresponds to assume the stress along the radial direction to be zero everywhere. Thus,

$$p = \sigma_3 = \frac{\lambda_3}{J} \frac{\partial \Psi}{\partial \lambda_3} \dots \dots (Eq. 3.3.)$$

And the stress in plane can be write as:

$$\begin{aligned} \sigma_1 &= \frac{\lambda_1}{J} \frac{\partial \Psi}{\partial \lambda_1} - p = \lambda_1 \frac{\partial \Psi}{\partial \lambda_1} - \lambda_3 \frac{\partial \Psi}{\partial \lambda_3} \\ \sigma_2 &= \lambda_2 \frac{\partial \Psi}{\partial \lambda_2} - p = \lambda_2 \frac{\partial \Psi}{\partial \lambda_2} - \lambda_3 \frac{\partial \Psi}{\partial \lambda_3} \dots \dots (Eq. 3.4.) \end{aligned}$$

$\sigma_1$  is equal to the in plane stress of the bulge membrane along the window size direction, and thus is the stress to be related to the pressure when pursuing the derivation of the bulge equation.

In most cases, as mentioned before, strain energy function  $\Psi$  is a function of the stretch invariants. Thus the stress-energy relation is recast by inducing the conversion of stretch and invariant:

$$\begin{aligned} I_1 &= \lambda_1^2 + \lambda_2^2 + \lambda_3^2 \\ I_2 &= \lambda_1^2 \lambda_2^2 + \lambda_2^2 \lambda_3^2 + \lambda_1^2 \lambda_3^2 \\ I_3 &= \lambda_1^2 \lambda_2^2 \lambda_3^2 = 1 \dots \dots (Eq. 3.5.) \end{aligned}$$

The derivative of strain energy to a stretch component is used to calculate stress, and can be recast as:

$$\begin{aligned} \frac{\partial \Psi}{\partial \lambda_1} &= \frac{\partial \Psi}{\partial I} \frac{\partial I}{\partial \lambda_1} = \frac{\partial \Psi}{\partial I_1} \cdot \frac{\partial I_1}{\partial \lambda_1} + \frac{\partial \Psi}{\partial I_2} \cdot \frac{\partial I_2}{\partial \lambda_1} \\ \frac{\partial \Psi}{\partial \lambda_2} &= \frac{\partial \Psi}{\partial I} \frac{\partial I}{\partial \lambda_2} = \frac{\partial \Psi}{\partial I_1} \cdot \frac{\partial I_1}{\partial \lambda_2} + \frac{\partial \Psi}{\partial I_2} \cdot \frac{\partial I_2}{\partial \lambda_2} \end{aligned}$$

$$\frac{\partial \Psi}{\partial \lambda_3} = \frac{\partial \Psi}{\partial \mathbf{I}} \frac{\partial \mathbf{I}}{\partial \lambda_3} = \frac{\partial \Psi}{\partial I_1} \cdot \frac{\partial I_1}{\partial \lambda_3} + \frac{\partial \Psi}{\partial I_2} \cdot \frac{\partial I_2}{\partial \lambda_3} \dots \dots (Eq. 3.6.)$$

The derivatives of invariants to different stretches are:

$$\begin{aligned} \frac{\partial I_1}{\partial \lambda_1} &= 2\lambda_1, & \frac{\partial I_1}{\partial \lambda_2} &= 2\lambda_2, & \frac{\partial I_1}{\partial \lambda_3} &= 2\lambda_3 \\ \frac{\partial I_2}{\partial \lambda_1} &= 2\lambda_1\lambda_2^2 + 2\lambda_1\lambda_3^2, & \frac{\partial I_2}{\partial \lambda_2} &= 2\lambda_2\lambda_1^2 + 2\lambda_2\lambda_3^2 \\ \frac{\partial I_2}{\partial \lambda_3} &= 2\lambda_3\lambda_1^2 + 2\lambda_3\lambda_2^2 \dots \dots (Eq. 3.7.) \end{aligned}$$

So the derivative of strain energy function to a stretch component is:

$$\begin{aligned} \frac{\partial \Psi}{\partial \lambda_1} &= \frac{\partial \Psi}{\partial I_1} \cdot \frac{\partial I_1}{\partial \lambda_1} + \frac{\partial \Psi}{\partial I_2} \cdot \frac{\partial I_2}{\partial \lambda_1} = \frac{\partial \Psi}{\partial I_1} \cdot 2\lambda_1 + \frac{\partial \Psi}{\partial I_2} \cdot (2\lambda_1\lambda_2^2 + 2\lambda_1\lambda_3^2) \\ \frac{\partial \Psi}{\partial \lambda_2} &= \frac{\partial \Psi}{\partial I_1} \cdot \frac{\partial I_1}{\partial \lambda_2} + \frac{\partial \Psi}{\partial I_2} \cdot \frac{\partial I_2}{\partial \lambda_2} = \frac{\partial \Psi}{\partial I_1} \cdot 2\lambda_2 + \frac{\partial \Psi}{\partial I_2} \cdot (2\lambda_2\lambda_1^2 + 2\lambda_2\lambda_3^2) \\ \frac{\partial \Psi}{\partial \lambda_3} &= \frac{\partial \Psi}{\partial I_1} \cdot \frac{\partial I_1}{\partial \lambda_3} + \frac{\partial \Psi}{\partial I_2} \cdot \frac{\partial I_2}{\partial \lambda_3} = \frac{\partial \Psi}{\partial I_1} \cdot 2\lambda_3 + \frac{\partial \Psi}{\partial I_2} \cdot (2\lambda_3\lambda_1^2 + 2\lambda_3\lambda_2^2) \dots \dots (Eq. 3.8.) \end{aligned}$$

Thus the stress-energy relationship can be rewrite as:

$$\begin{aligned} \sigma_1 &= \lambda_1 \frac{\partial \Psi}{\partial \lambda_1} - \lambda_3 \frac{\partial \Psi}{\partial \lambda_3} \\ &= \lambda_1 \left[ \frac{\partial \Psi}{\partial I_1} \cdot 2\lambda_1 + \frac{\partial \Psi}{\partial I_2} \cdot (2\lambda_1\lambda_2^2 + 2\lambda_1\lambda_3^2) \right] \\ &\quad - \lambda_3 \left[ \frac{\partial \Psi}{\partial I_1} \cdot 2\lambda_3 + \frac{\partial \Psi}{\partial I_2} \cdot (2\lambda_3\lambda_1^2 + 2\lambda_3\lambda_2^2) \right] \\ &= \frac{\partial \Psi}{\partial I_1} \cdot 2(\lambda_1^2 - \lambda_3^2) + \frac{\partial \Psi}{\partial I_2} \cdot 2\lambda_2^2(\lambda_1^2 - \lambda_3^2) \\ \sigma_2 &= \lambda_2 \frac{\partial \Psi}{\partial \lambda_2} - \lambda_3 \frac{\partial \Psi}{\partial \lambda_3} = \frac{\partial \Psi}{\partial I_1} \cdot 2(\lambda_2^2 - \lambda_3^2) + \frac{\partial \Psi}{\partial I_2} \cdot 2\lambda_1^2(\lambda_2^2 - \lambda_3^2) \dots \dots (Eq. 3.9.) \end{aligned}$$

The derivative of invariants to stretches are separated because they are the fixed terms for different strain-energy models. This corresponds to a practical choice when the solution has to be implemented numerically.

### 3.2 Geometrical general situation

In continue, the traditional analytical treatment presented in Chapter 2 will be reviewed to introduce the non-linear hyperelastic behavior described in the previous paragraph.

The geometry of a sector circular is used to calculate the strain of a bulge membrane in the window size direction, therefore, Eq.2.3. can be applied here. However, the assumption was made only on relatively small deflection, which would not be appropriate for an elastomer. A more general expression of the radius as a function of the deflection and the window size reads

$$R = \frac{(h^2 + a^2)}{2h} \dots \dots (Eq. 3.10.)$$

The stretch along the window size direction can be expressed by

$$\lambda_1 = R\theta/a \dots \dots (Eq. 3.11.)$$

Where  $\theta$ , as can be seen from the geometry, is a function of R and a

$$\theta = \arcsin a/R = \arcsin 2ah/(a^2 + h^2) \dots \dots (Eq. 3.12.)$$

Thus the stretch can be expressed as a function of  $h$  and  $a$  as follows

$$\lambda_1 = \frac{R\theta}{a} = \frac{h^2 + a^2}{2ah} \arcsin \frac{2ah}{a^2 + h^2} \dots \dots (Eq. 3.13.)$$

### 3.3 Hyperelastic bulge modeling- circular window

As illustrated in the previous chapter, when the bulge window features a circular shape, the stress in the plane of the membrane is equi-biaxial. Thus, when the sample is bulged,  $\sigma_1 = \sigma_2$ , and the membrane is equally stretched along this two direction. That is:  $\lambda_1 = \lambda_2$ . Recalling the hypothesis of material incompressibility, it can be stated that that  $\lambda_1\lambda_2\lambda_3 = 1$ , therefore when setting  $\lambda_1 = \lambda$ , the following relations hold

$$\lambda_1 = \lambda, \quad \lambda_2 = \lambda, \quad \lambda_3 = \frac{1}{\lambda^2} \dots \dots (Eq. 3.14.)$$

Using these results in the stress/stretch relation obtained in the previous section (Eq.3.8.), one can get:

$$\begin{aligned} \sigma_1 &= \frac{\partial \Psi}{\partial I_1} \cdot 2(\lambda_1^2 - \lambda_3^2) + \frac{\partial \Psi}{\partial I_2} \cdot 2\lambda_2^2(\lambda_1^2 - \lambda_3^2) \\ &= 2 \frac{\partial \Psi}{\partial I_1} \left( \lambda^2 - \frac{1}{\lambda^4} \right) + 2 \frac{\partial \Psi}{\partial I_2} \left( \lambda^4 - \frac{1}{\lambda^2} \right) \dots \dots (Eq. 3.15.) \end{aligned}$$

Recalling the bulge equation for circular windows from the previous chapter (Eq.2.10.), one can write:

$$\sigma = \frac{pR}{2t} = \frac{p(a^2 + h^2)}{4th} \dots \dots (Eq. 3.16.)$$

Here,  $\sigma = \sigma_1$ . Also, unlike in the linear elastic case, where thickness is a constant, in hyperelastic materials, thickness evolves as the bulge pressure build up. If the original thickness is  $t_0$ , then the current thickness can be obtained as:  $t = t_0 \cdot \lambda_3 = t_0/\lambda^2$ . So one can rewrite the previous equation as:

$$\begin{aligned} p &= \frac{4\sigma_1 th}{a^2 + h^2} = 8 \cdot \frac{t_0 h}{(a^2 + h^2)\lambda^2} \\ &\cdot \left[ \frac{\partial \Psi}{\partial I_1} \left( \lambda^2 - \frac{1}{\lambda^4} \right) + 2 \frac{\partial \Psi}{\partial I_2} \left( \lambda^4 - \frac{1}{\lambda^2} \right) \right] \dots \dots (Eq. 3.17.) \end{aligned}$$

That is the bulge equation for hyperelastic material under circular window. In order to recast it as a proper pressure/deflection relation, one should substitute  $\lambda$  using the equation from last section (Eq.3.13.).

### 3.4 Hyperelastic bulge modeling- rectangular window

For the rectangular window model, the plane-strain condition holds rather than equi-biaxial stress. That is  $\varepsilon_1 \neq 0$ ,  $\varepsilon_2 = 0$ .

As concerns stretches, that means:  $\lambda_1 \neq 1$ ,  $\lambda_2 = 1$ . Set  $\lambda_1 = \lambda$ , therefore

$$\lambda_1 = \lambda, \quad \lambda_2 = 1, \quad \lambda_3 = \frac{1}{\lambda} \dots \dots (Eq. 3.18.)$$

Using the expression of stretches in plane strain condition in the stress-stretch relation one obtains:

$$\begin{aligned} \sigma_1 &= \frac{\partial \Psi}{\partial I_1} \cdot 2(\lambda_1^2 - \lambda_3^2) + \frac{\partial \Psi}{\partial I_2} \cdot 2\lambda_2^2(\lambda_1^2 - \lambda_3^2) = 2 \frac{\partial \Psi}{\partial I_1} \left( \lambda^2 - \frac{1}{\lambda^2} \right) + 2 \frac{\partial \Psi}{\partial I_2} \left( \lambda^2 - \frac{1}{\lambda^2} \right) \\ &= 2 \left( \frac{\partial \Psi}{\partial I_1} + \frac{\partial \Psi}{\partial I_2} \right) \left( \lambda^2 - \frac{1}{\lambda^2} \right) \dots \dots (Eq. 3.19.) \end{aligned}$$

Referring back to Eq.2.17., the bulge equation for rectangular window can be rewrite as:

$$\sigma = \frac{pR}{t} = \frac{p(a^2 + h^2)}{2th} \dots \dots (Eq. 3.20.)$$

Like in the previous case, thickness changes as the bulge evolves.  $t = t_0 \cdot \lambda_3 = t_0/\lambda$ .

Thus the bulge equation for hyperelastic material under rectangular window is:

$$p = \frac{2\sigma_1 th}{a^2 + h^2} = 4 \cdot \frac{t_0 h}{(a^2 + h^2)\lambda} \cdot \left( \frac{\partial \Psi}{\partial I_1} + \frac{\partial \Psi}{\partial I_2} \right) \left( \lambda^2 - \frac{1}{\lambda^2} \right) \dots \dots (Eq. 3.21.)$$

Here, the substitution of stretch to window size and deflection height (Eq.3.13.) still holds.



### 3.5 Hyperelastic bulge modeling- with constitutive modeling

The bulge equation for hyperelastic materials was developed in the previous section. The strain energy function assumes a different expression depending on the specific hyperelastic model to be used, thus to finish the modeling, the most popular hyperelastic strain energy potentials for rubber like materials are introduced here.

Noteworthy, the only terms to be instanced when selecting a specific strain energy function correspond to the derivatives of the latter with respect to the stretch invariants. To be less tedious, only  $\frac{\partial \psi}{\partial I_1}$  and  $\frac{\partial \psi}{\partial I_2}$  would be listed for each model, which are the only relevant derivative appearing in the hyperelastic bulge equation. In continue, the derivatives of the strain energy function with respect to the stretch invariants are presented for five popular hyperelastic models.

#### 3.5.1 Construction of hyperelastic bulge equation with with constitutive models

##### General terms for different constrain situation

The bulge equation for hyperelastic material have terms that change for different cases-the invariants. Invariant is a function of stretch, and as can be seen above, stretch differs from case to case. Thus here listed the invariants according to different cases. When using the hyperelastic bulge equation, one should put the proper substitution to invariants according to the actual case.

- 1) Circular window case-equibiaxial situation

$$\lambda_1 = \lambda, \quad \lambda_2 = \lambda, \quad \lambda_3 = \frac{1}{\lambda^2}$$

$$I_1 = \lambda_1^2 + \lambda_2^2 + \lambda_3^2 = 2\lambda^2 + \frac{1}{\lambda^4}$$

$$I_2 = \lambda_1^2 \lambda_2^2 + \lambda_2^2 \lambda_3^2 + \lambda_1^2 \lambda_3^2 = \lambda^4 + \frac{2}{\lambda^2} \dots \dots (Eq. 3.22.)$$

- 2) Rectangular window case-plane strain situation

$$\lambda_1 = \lambda, \quad \lambda_2 = 1, \quad \lambda_3 = \frac{1}{\lambda}$$

$$I_1 = \lambda_1^2 + \lambda_2^2 + \lambda_3^2 = \lambda^2 + 1 + \frac{1}{\lambda^2}$$

$$I_2 = \lambda_1^2 \lambda_2^2 + \lambda_2^2 \lambda_3^2 + \lambda_1^2 \lambda_3^2 = \lambda^2 + \frac{1}{\lambda^2} + 1 \dots \dots (Eq. 3.23.)$$

3) Uniaxial situation (see the potential usage in next section.)

$$\lambda_1 = \lambda, \quad \lambda_2 = \frac{1}{\sqrt{\lambda}}, \quad \lambda_3 = \frac{1}{\sqrt{\lambda}}$$

$$I_1 = \lambda_1^2 + \lambda_2^2 + \lambda_3^2 = \lambda^2 + 2/\lambda$$

$$I_2 = \lambda_1^2 \lambda_2^2 + \lambda_2^2 \lambda_3^2 + \lambda_1^2 \lambda_3^2 = 2\lambda + \frac{1}{\lambda^2} \dots \dots (Eq. 3.24.)$$

### Derivatives of different constitutive hyperelastic function to invariants

#### Arruda-Boyce form

$$\Psi = \mu \left[ \frac{1}{2} (I_1 - 3) + \frac{1}{20\lambda_m^2} (I_1^2 - 9) + \frac{11}{1050\lambda_m^4} (I_1^3 - 27) + \frac{19}{7000\lambda_m^6} (I_1^4 - 81) \right. \\ \left. + \frac{519}{673750\lambda_m^8} (I_1^5 - 243) \right]$$

$$\frac{\partial \Psi}{\partial I_1} = \mu \left( \frac{1}{2} + \frac{2}{20\lambda_m^2} I_1 + \frac{11 \times 3}{1050\lambda_m^4} I_1^2 + \frac{19 \times 4}{7000\lambda_m^6} I_1^3 + \frac{519 \times 5}{673750\lambda_m^8} I_1^4 \right) \dots \dots (Eq. 3.25.)$$

Here,  $\mu, \lambda_m$  are temperature dependent material parameters.

#### Mooney-Rivlin form

$$\Psi = C_{10}(I_1 - 3) + C_{01}(I_2 - 3)$$

$$\frac{\partial \Psi}{\partial I_1} = C_{10}, \quad \frac{\partial \Psi}{\partial I_2} = C_{01} \dots \dots (Eq. 3.26.)$$

#### Neo-Hookean form

$$\Psi = C_{10}(I_1 - 3)$$

$$\frac{\partial \Psi}{\partial I_1} = C_{10} \dots \dots (Eq. 3.27.)$$

### Polynomial form (N=2)

$$\Psi = \sum_{i+j=1}^N C_{ij} (I_1 - 3)^i (I_2 - 3)^j$$

$$\frac{\partial \Psi}{\partial I_1} = C_{10} + C_{11}(I_2 - 3) + 2C_{20}(I_1 - 3)$$

$$\frac{\partial \Psi}{\partial I_2} = C_{01} + C_{11}(I_1 - 3) + 2C_{02}(I_2 - 3) \dots \dots (Eq. 3.28.)$$

### Yeoh form

$$\Psi = C_{10}(I_1 - 3) + C_{20}(I_1 - 3)^2 + C_{30}(I_1 - 3)^3$$

$$\frac{\partial \Psi}{\partial I_1} = C_{10} + 2C_{20}(I_1 - 3) + 3C_{30}(I_1 - 3)^2 \dots \dots (Eq. 3.29.)$$

### **3.5.2 Potential usage of the uniaxial hyperelastic equation**

A potential use of the hyperelastic bulge equation developed in the previous section consists in the combination with uniaxial stress/strain data to identify the most suitable hyperelastic model to describe the response of a non-linear elastic material. It enables the usage of uniaxial tensile test as substitution of profilometer to obtain strain control mechanism. (Profilometer experimental detail given in Chapter 5)

Specifically, one can perform a uniaxial tensile test, and perform a numerical fitting to obtain the material constitutive parameters. This can be done provided that the hyperelastic stress/strain response upon uniaxial stretch is known from experimental data. Recalling from previous section, the general stress-stretch relation (Eq.3.9.) is:

$$\sigma_1 = \frac{\partial \Psi}{\partial I_1} \cdot 2(\lambda_1^2 - \lambda_3^2) + \frac{\partial \Psi}{\partial I_2} \cdot 2\lambda_2^2(\lambda_1^2 - \lambda_3^2)$$

For uniaxial stress, the membrane will be stretched in one dimension only, and experience contraction along the remaining two dimensions. This means

$$\lambda_1 = \lambda, \quad \lambda_2 = \frac{1}{\sqrt{\lambda}}, \quad \lambda_3 = \frac{1}{\sqrt{\lambda}} \dots \dots (Eq. 3.30)$$

So the stress-stretch relation for uniaxial strains reads as

$$\sigma_1 = 2 \frac{\partial \Psi}{\partial I_1} \left( \lambda^2 - \frac{1}{\lambda} \right) + 2 \frac{\partial \Psi}{\partial I_2} \left( \lambda - \frac{1}{\lambda^2} \right) \dots \dots (Eq. 3.31)$$

By fitting the experimental uniaxial stress/strain curve with hyperelastic models and Eq.3.31, best-fitting material parameters are obtained. One can insert the material parameters into the hyperelastic bulge equation to obtained pressure-deflection behavior of the sample material, then a pressure-strain relation under bulge test needed for the crack opening study is ready to be used.

### 3.6 Conclusion and discussion

Substrate material used in this study is PDMS, which is an elastomer, does not comply to the original bulge equation which is constructed mainly for materials with linear elastic response. Thus hyperelastic bulge equation is developed in this chapter. With the usage of hyperelastic bulge equation, one can perform characterization of rubber-like hyperelastic materials under bulge test with in-situ laser profilometer, which will be illustrated in detail in Chapter 5. By fitting experimental data from bulge test under profilometer, best-fitting material parameters can be yielded. Pressure-strain control mechanism can also be obtained by the set of best-fitting material parameters from hyperelastic bulge equation, which enables crack opening study in bulge test under in-situ optical microscopy. Experimental detail will be given in Chapter 6. It is the main experiment procedure of this study: performing bulge test with in-situ profilometer to get experimental p-h behavior – fit p-h behavior with hyperelastic bulge equation developed in this chapter – use best-fitting parameters to construct pressure-strain response – conduct crack opening study with bulge test under in-situ optical microscope with a known strain control.

Uniaxial tensile stress is also mentioned in this chapter, for the possible application in experimental cooperation. One can perform a uniaxial tensile test on the same material that would be used in bulge device, fit the data with hyperelastic model to give parameters and then use them in the hyperelastic bulge equation. It is an optional way to obtain material properties experimentally and thus to give a better reference to pressure-strain relationship, which serves the purpose of this study.

## 4 Development of the bulge test setup

A device setup was developed to perform bulge tests on Au/PDMS samples for stretchable electronics applications. During the development of the setup, some practical issues implied the need of several reviews and prototypes, before the final version of the device was achieved. In continue, only the final version of the bulge test device will be illustrated, and the key issues that need to be considered during the manufacturing will be pointed out.

The window of the manufactured bulge device is a circular one, 1mm in diameter. The choice of size and shape of the window is made under consideration of available manufacturing facilities in the lab, as well as the material choice for the device. The possible pressure range the bulge test setup can provide is 0-1.5 PSI.

The bulge test setup is used under two different experiment instrument during this study, an in-situ laser profilometer and an inverted optical microscope. Bulge test with in-situ profilometer enables characterization of the elastomer substrate, by fitting the pressure-deflection response with hyperelastic bulge equation developed in previous chapter. Fitting parameters can be used to construct pressure-strain control of the bulge device for this material. The characterized sample is then used under bulge test with in-situ optical microscope. Intuitionistic crack opening study can be conducted combined with the pressure-strain control known from the profilometer experiment. In this manner, the goal of this study, namely, the crack evolution study of Au/PDMS sample through bulge testing, is achieved.

## 4.1 Sample preparation [36]

The gold on PDMS samples used in this study were fabricated by Tinku and co-workers at the research institute Fondazione Bruno Kessler (FBK, Trento, IT). In continue, a brief introduction on the material properties and the fabrication techniques will be given. A detailed description of the fabrication process can be found in [36,37].

PDMS has a significantly different thermal expansion coefficient than the rest of the layers in the micro fabrication routine. This may lead to lots of cracks and adhesion issues. Thus special caution should be paid to minimize the thermal shocks steps during the process. The direct contact of PDMS and photoresist was first avoided, so as to avoid thermal shocks to the polymer. The fabrication steps were as follows:

- cleaning and rinsing of Si wafers to be used a substrates for the subsequent spin coating of PDMS
- silanization of the wafers for easy removal of PDMS- PDMS (10:1 ratio) spin-coated on wafer at 500 RPM for 60 sec.(thickness of PDMS~150 $\mu$ m)
- coated wafers were kept 2 hours in oven at 80°C for polymer curing
- an Oxygen (O<sub>2</sub>) plasma treatment was used to to enhance the surface adhesion

## 4.2 Device Manufacture

The main body of the device is manufactured in the workshop of the Laboratory of mechanics of Biological Structures (LabS) in Politecnico di Milano. The component choice of the device and its size are decided with main consideration of the available manufacturing facilities.

### 4.2.1 Overview of setup

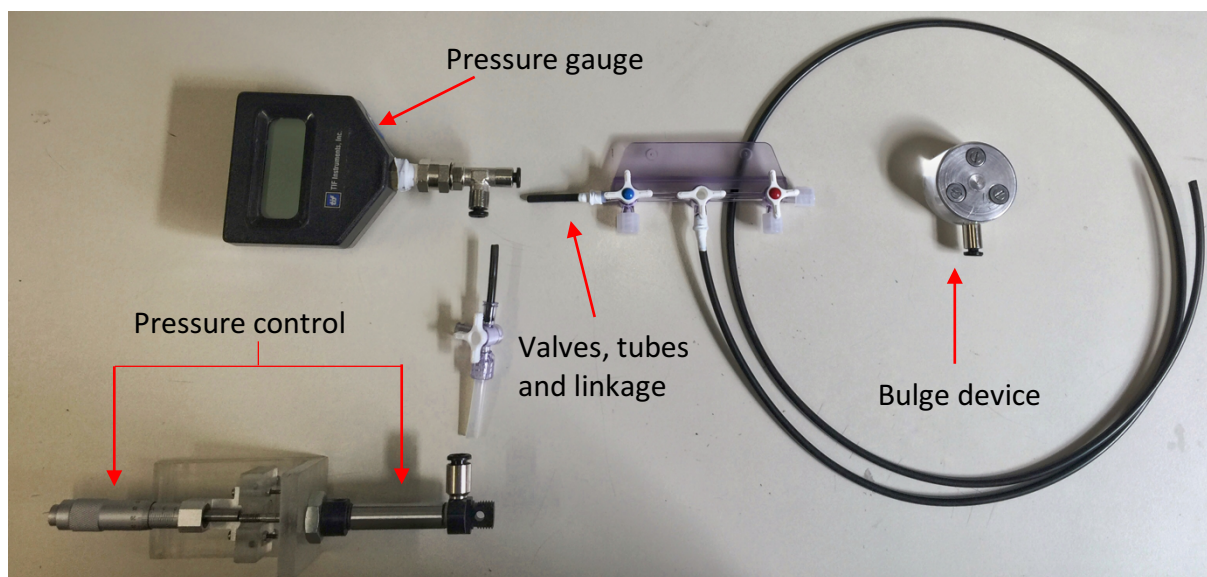


*Fig.4.1. Overall setup of bulge test*

The overall bulge test setup is shown in Fig.4.2. The most important components are: pressure provider system, pressure sensor, linkage system and the bulge device.

Normal pressure providing system for bulge test can be divided into two groups: gas provider and liquid provider. Liquid provider are used too meet larger pressure requirement for stiffer materials, which is not the case of current interest. Also, the filling procedure of the setup with liquid providers is normally associated with the issue of air-bubble entrapment, which complicates the practical use of this solution. Thus, gas was chosen to be the pressure provider. A pneumatic cylinder plus a micrometric screw are used in the setup in order to compress the volume entrapped within the setup components and the sample, therefore building-up pressure. A syringe, which is not shown in the picture, was also used to pump in air to enable the repeated



use of the pneumatic cylinder compression range within a single test, as it will be illustrated in the later sections.

For pressure sensor, a pressure gauge from TIF Instruments Inc. is used. The measuring unit is psi, with range 0-100 PSI.

The linkage system is carried out by two plastic valves and a proper combination of tubes. Two valves are used to allow the pneumatic decoupling between the pressure gauge and either the pressure cylinder or the bulge test device, when needed. Tubes should be as narrow as possible, so as to minimize the volume to be compressed, therefore maximizing the pressure build-up for a given micrometer-screw turn.

Fig 4.2. shows the overview of the bulge test device. Details will be shown later.

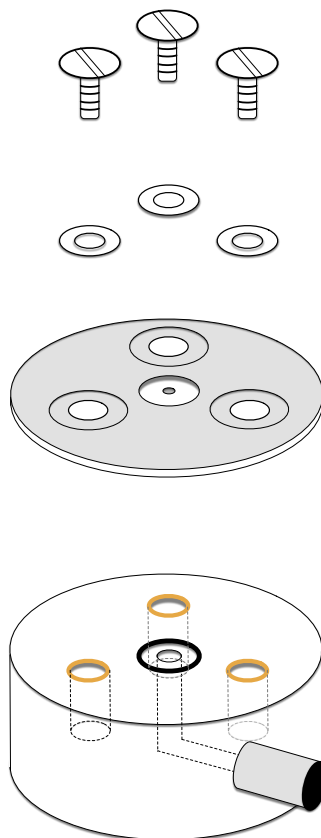


*Fig.4.2. Overview of bulge test device*

### 4.2.2 Cap manufacturing

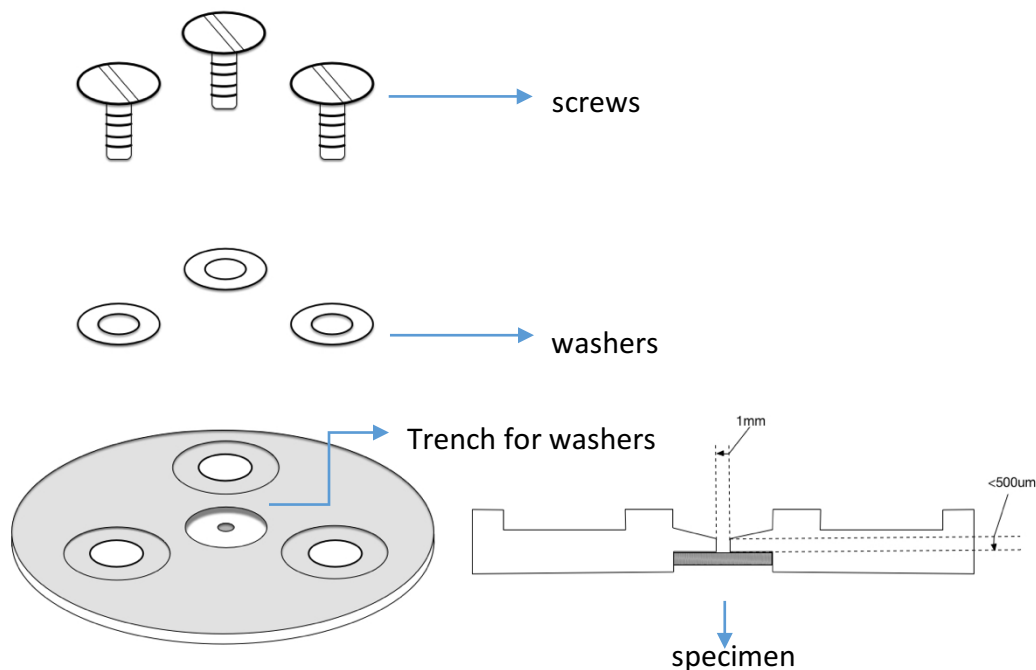


Fig.4.3. Schematic illustration of cap alignment

Three trenches for washers are fabricated also on the cap. The usage of washer increases the tightening of the screw head and the cap, which then ensures a better sealing condition. The central holes of the washers are shaped slightly conically, so as to fit the conical screw and made them disappear below the surface of the cap when fixing heads even better. But this depends on the type of screws that would be used in the device. We choose the screws with conical heads. The finished product is shown in Fig.4.4.

The schematic illustration of cap alignment is shown in Fig.4.3. The alignment includes: screws, washers and the cap. Only circular windows are made during this project, since using a proper drill tip is possible to fabricate a circular window, while for rectangular and square windows, a mill tip with proper size would have been needed, which was not available within the fabrication facilities. Nevertheless, for the reason that rectangular windows provide constrains for plane strain condition, which will be more suitable for stiffer materials. But one can fabricate rectangular or even square windows under similar fabrication procedure.

The cap is fabricated from a piece of metal with thickness less than 2mm. In the central region of the cap, an opening blind cavity is fabricated to reduce the depth from the top to the specimen,

so that the device is applicable for experiment under in combination with equipment operating at relatively short working distance with respect to the surface of interest (namely, the laser profilometer and the optical microscope). The laser profilometer has a working distance below 1.5mm, therefore a slope of the opening is made on purpose to allow the laser head to approach closer to the specimen without hitting the outer ridge fringe. The reason for choosing metal rather than PMMA as for the rest of the setup relies on the fact that, in order to comply the aforementioned constraints, the cap thickness is rather small in the region where the sample is clamped. Therefore, using metal ensured higher stiffness of the constraint as compared to that of the sample (despite the slender geometry of the constraint).

During application under laser profilometer, once the membrane is detected, the laser head moves up and down in the distance of 500 microns, to determine its position. So the distance between the top of opening and the specimen at unbulged condition should be less than 500 microns. But it is difficult to achieve on a single side fabrication, otherwise the slope is too large. The specimen stage on the backside of the cap is made for this purpose. The diameter of the stage can be fixed to the value of that of the specimen, such that it is easier to center the specimen. Additionally, with the limitation of working distance, only the circular cap with 500 $\mu$ m in radius can be used to obtain full range p-h experimental data. Any window larger than this will result in deflection height off the promising range, thus bulge membrane of only a partial pressure range will be measured.

Only a window of 1mm in diameter is made as a metal, though several caps were tried out with other window sizes from PMMA. Metal is finally chosen instead of PMMA like the rest of the device, to ensure the compatibility with the screws head, otherwise the cap would be blended after a few times of usage.

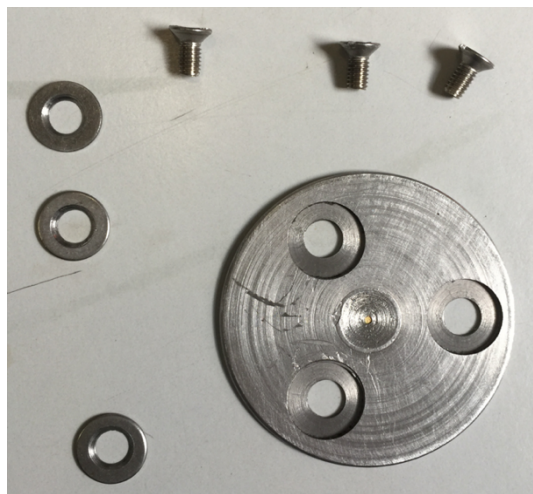


*Fig.4.4. Finished product of cap*

### 4.2.3 Main body manufacturing

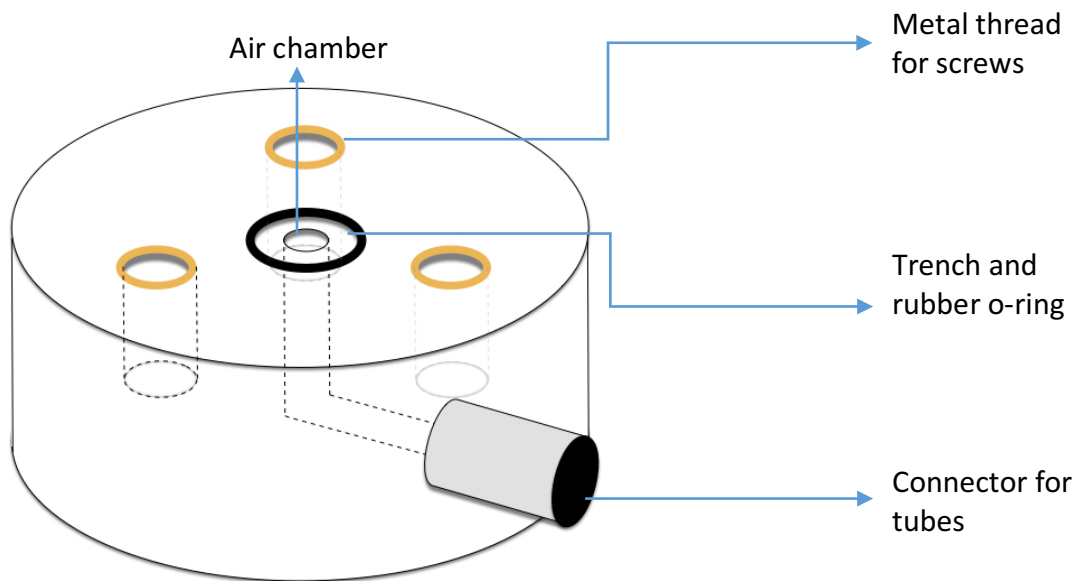


*Fig.4.5. Schematic illustration of device chamber*

The schematic illustration of the main body of the device is shown in Fig.4.5. The device is fabricated with PMMA, which is a cheap, easy-to-manufacture material. The main body of the device include several important components, those are: air chamber, trench and o-ring, metal thread for screws and the connector for tubes.

The device is made as a cylinder, and the air chamber is constructed in the center by intersecting two orthogonal cavities obtained by means of a 2mm drill tip. Air chamber does not have size limitation, due to the fact that the samples is mechanically constrained by the cap, instead. But, as already explained for the tubes, in order to have more effective pressure build up, the chamber should be as narrow as possible.

The bottom of the cylindrical chamber links to a connector for tubes. This is a rapid-fix pneumatic metal connector featuring an o-ring on the thread. It provides excellent sealing. A trench and a threaded hole are manufactured in the PMMA main body, to make ensure conformal and tight contact (and therefore sealing) between the connector and the device wall.

A trench outside the air chamber is fabricated for the placement of an o-ring. The o-ring is needed to improve sealing ability. The trench should be half of the o-ring thickness in depth, and slightly smaller than the o-ring in diameter and width. While the o-ring is being placed, it

should be a little bit stretched spherically and compressed along width so as to be fixed at the position. When fixing the cap on top, the o-ring should be compressed drastically and no space should exist between cap and device.

The threads for screws are made from metal. In a preliminary attempt, threads for screws were obtained directly in the PMMA main body, but after fixing/unfixing the screws a few times, the threads got significantly damaged. Therefore, a threaded metal sleeve was used to enhance the reliability of the device with regards to the task of fixing/unfixing the cap.

Fig.4.6. shows the finished product of the main body of the device.

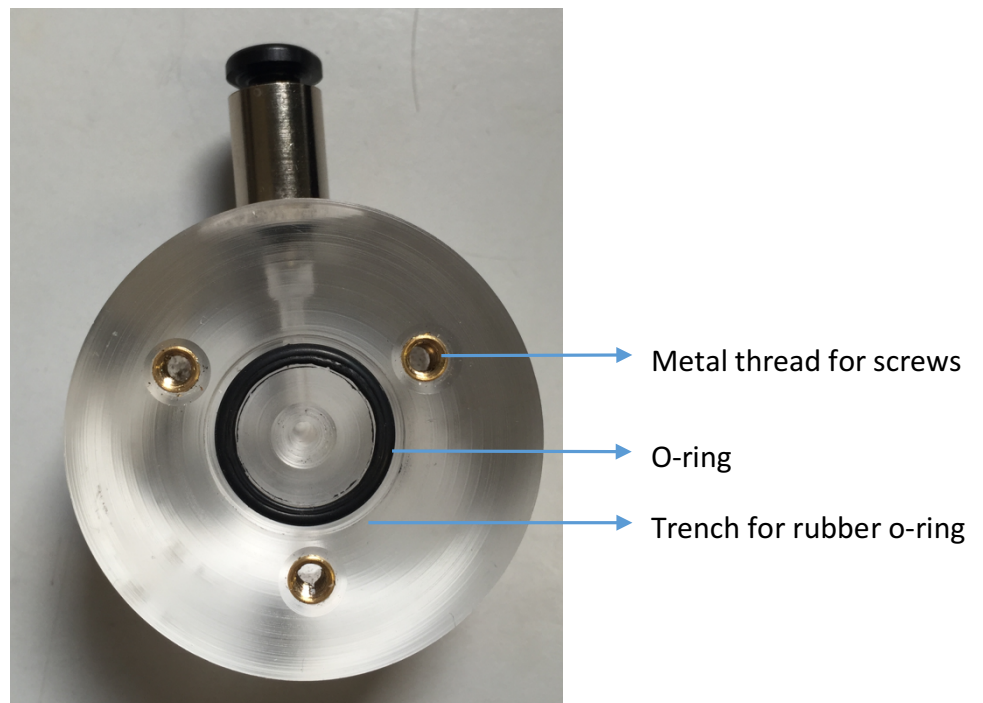


*Fig.4.6. Finished product of main body of the device*

#### 4.2.4 Pressure build up and control

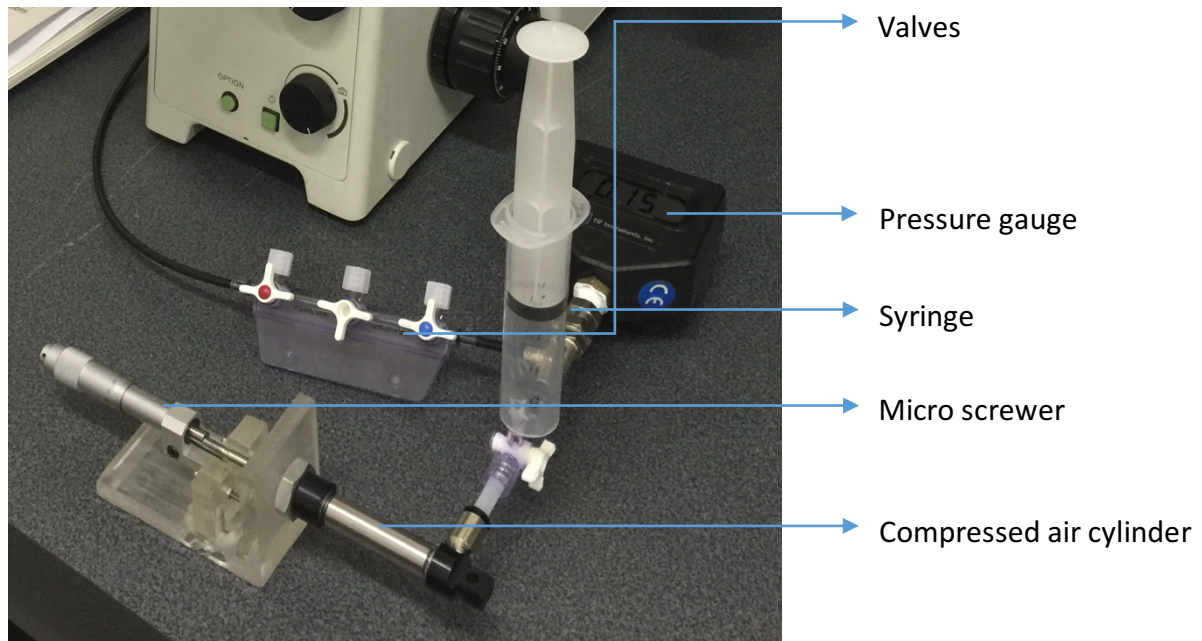


Fig.4.7. Actual setup of pressure providing and controlling system

For pressure providing system, the syringe is the main air provider. It was used to pump in air to a certain value (displayed by the pressure gauge), and close the valve on its side. Then a pneumatic cylinder (Air Work Pneumatic Equipment) is used to adjust gradually the pressure until it reaches the one desired. We used a micrometric screw to move the piston of the pneumatic cylinder. The construction of the cylinder is shown in Fig.4.8.

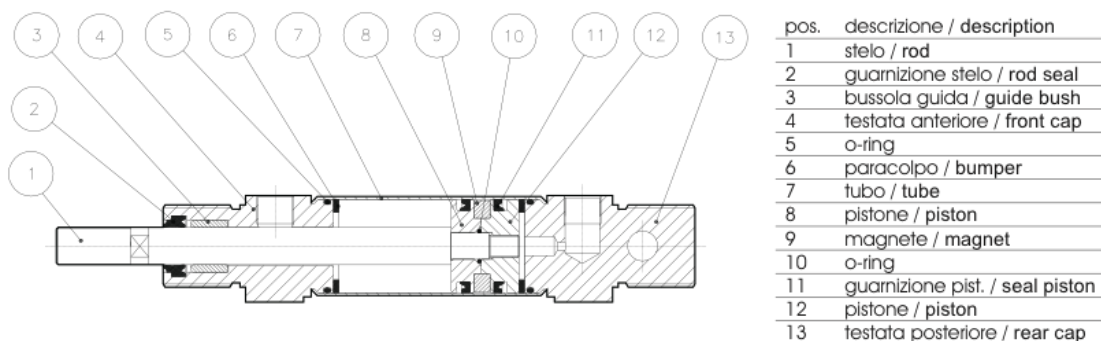


Fig.4.8. Construction of the compressed air cylinder

For pressure sensing, a pressure gauge from TIF Instrument Inc. is used. The pressure gauge measures the pressure in the unit of PSI (1 PSI~ 6.9 kPa). The measuring range is from 0--100 PSI, with resolution of 0.01 PSI. The hexagonal nut of the pressure gauge must be tightened while mounting to the system. An envelope of Teflon tape should also be applied on the thread, in order to improve the sealing.

For pressure controlling system, several valves and a micrometric screw is involved. As concerns the micrometric screw, this was used not only to push the piston of the compressed air chamber cylinder, but also to finitely adjust pressure. Two three-way valves are also used to better control the pressure and avoid leakage as much as possible.

One of them is placed at the joint of device and pressure gauge (valve 1), the other is at the joint of pressure gauge and the pumping system (valve 2), that is, the syringe and air compressed chamber cylinder. During the air-repumping by the syringe when the full range of piston runs out, the valve 1 should be closed to the bulge device, pressure gauge and the pressure providing system remains linked. While adjusting finitely the pressure, the side of syringe should be closed, and after that, the whole pressure providing system should be isolated by turning off valve 2. In this way,

- The chance of leakage from the pressure providing system is minimized during the bulge test
- It is possible to exploit the compressibility range of the pneumatic cylinder repeatedly, therefore achieving relatively high pressure build-up despite the limited range of motion of the piston in the pneumatic cylinder



### 4.3 Specimen preparation and mounting



*Fig.4.9. A specimen mounted on the specimen stage of the backside of cap*

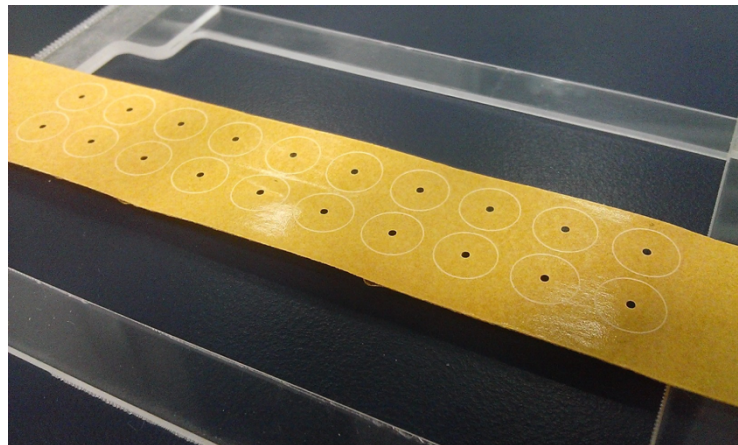


*Fig.4.10. Laser cut and marked double layer tape*

The specimen includes a small piece of sample and a tape to hold it beneath the cap. Tape is laser cut to provide precision while attaching the sample to the cap.

The fabrication on the tape is very important. The tape is a double sided tape, the top side is for adhesion to the cap, the bottom side is for sticking the Au/PDMS sample. A central hole



with a diameter exactly equal to that of the cap window and a larger, concentric mark are obtained by laser cutting. Fig 4.11. shows the finished tape after laser cut.

A small Au/PDMS sample should be then mounted on the tape. While peeling out the sample from the silicon substrate where it is normally stored, the user should pay extreme care, in order to avoid inducing cracks in the deposited Au layer before performing the test. The sample should be facing the tape with the Au coated side.

After all alignment of the specimen, the cap should be closed up by fixing in the screws. Special caution should be paid to the storage of the cap while the specimen is mounted on the cap but not on the device yet. Mechanical damage and chemical contamination should be avoided.

## 5 Bulge test with in-situ laser profilometry

To study crack opening corresponding to strain history of the Au/ PDMS samples, we should have control on strain loading. The realization of bulge test device enables an indirect strain control by manipulating the applied pressure and constraining the window size. As discussed in Chapters 2 and 3, the deflection height of the bulged membrane is a direct consequence of internal pressure, but from the bulge equation modelling we can derive the corresponding strain. Thus, to understand how the strain loading is controlled, first the pressure/deflection relation of a specimen at specific window size has to be addressed.

Bulge tests were performed under a laser profilometer to obtain deformed profiles under each specific pressure. By computing the deflection height from the profile and relate it to pressure, the desired pressure/deflection relation is obtained. The strain loading control then can be fully understood and is ready to apply on the crack opening study under in-situ optical microscopy, which will be described in Chapter 6.

## 5.1 Introduction of laser profilometry [38]

A laser profilometer is generally used for quantitative recognition and recording of micro-topography of a surface. The working principle of the laser profilometer relies on determining the relative distance between the sample surface and the scanning head by searching for the focus point of the laser.

The laser is directed to the sample being measured, then reflected. The reflected light is then directed to a prism by a beam splitter, after which the laser is imaged as a pair of spots on a set of photodiodes that are not arranged at the moment.

The setup is then arranged. When both diodes are equally illuminating, it indicates the precise focus distance from the sample. As a consequence, if the distance between the sample and the objective lens changes by a certain amount, the imaged focus point will be changed and the illumination of the diodes will no longer be equal.

This results in a focus measurement error that is generated by a differential amplifier. In order to perform an accurate measurement, both the spot size and its subsequent light distribution must be kept as constant.

A control circuit is used to manage this. It monitors the focus error and moves the objective lens according to the feedback changes in the distance between objective lens and sample. The objective lens are moved by a coil and magnet arrangement. This -movement is recorded by a light barrier measurement system which then yield the change of focal distance over the sample surface, that is, the sample topography.

The instrument used in the measurement in this study is an UBM Laser Profilometer. The specifications of the particular used instrument read as follows: a linear spot of diameter of  $1\mu\text{m}$ , a tolerable inclination of  $\pm 15^\circ$ , a measurement range  $\pm 500\mu\text{m}$ , and a vertical resolution  $10\text{nm}$ . The illustration of the measurement principles is shown in Fig.5.1.

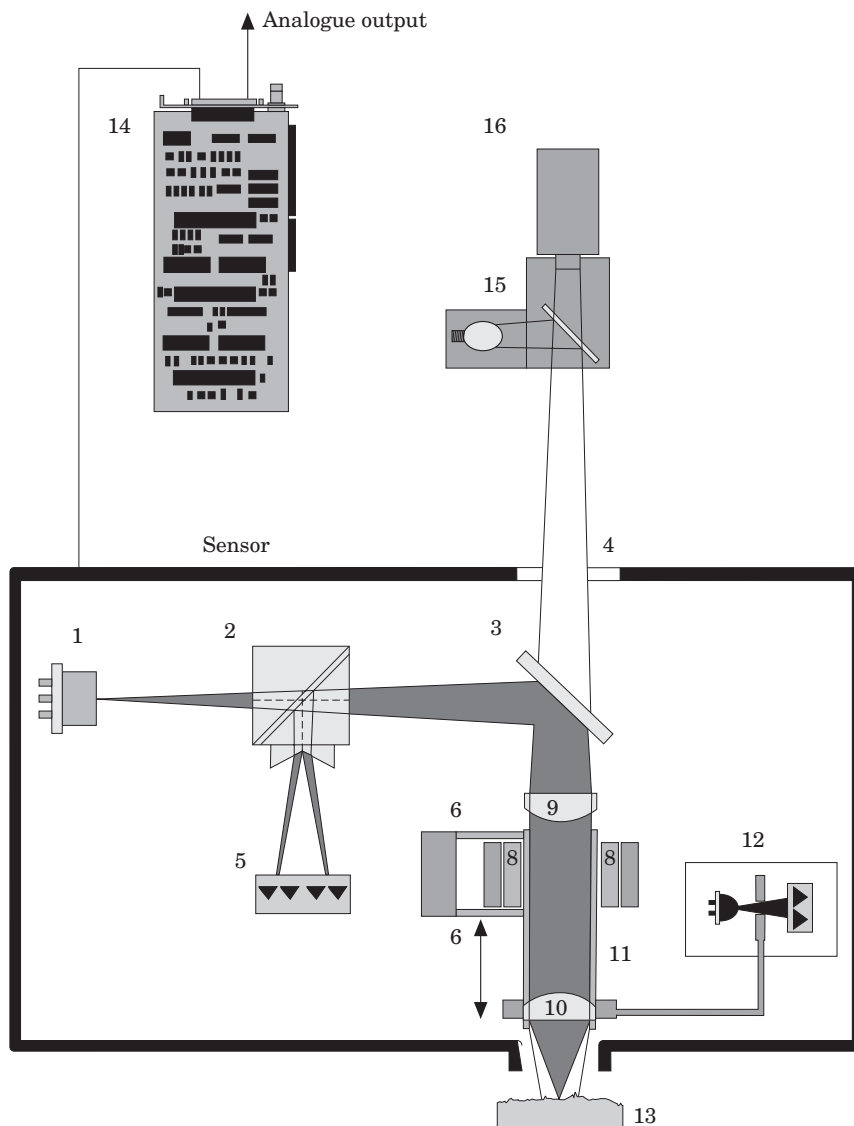


*Fig.5.1. Illustration of the measurement principle of the UBM laser profilometer. (1) Laser diode, (2) prism with beam splitter, (3) beam splitter, (4) window, (5) photodiodes, (6) leaf spring, (7) coil, (8) magnet, (9) collimator lens, (10) objective, (11) tube, (12) light barrier measurement system, (13) measurement object, (14) PC board, (15) microscope with illumination, (16) CCD camera.*

## 5.2 Setup description

The overall setup is shown in Fig.5.2.

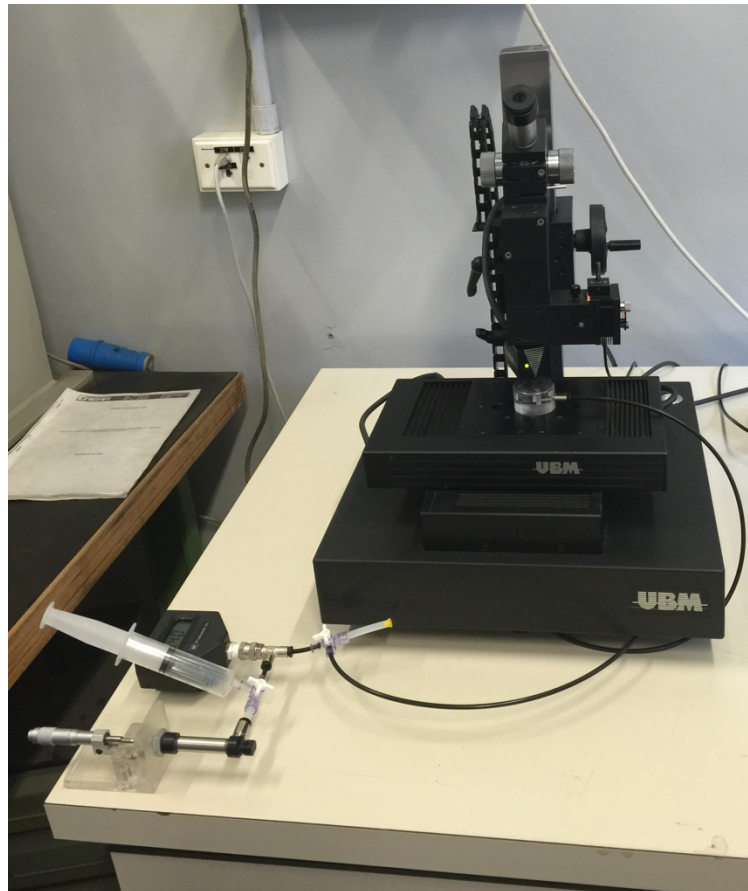


*Fig.5.2. Experimental setup for bulge test with in-situ profilometry*

## 5.3 Experiment Protocol

The experiment is conducted under the following protocol:

- 1) Setup the bulge test setup as illustrated in Fig.4.1.  
The cap is specially designed and fabricated for the application under laser profilometer. Radius of the window is also limited under consideration of promising working distance range. Detail reasoning is illustrated in Section 4.2.2.
- 2) Check the sealing condition of the device.  
The scanning to obtain the profile of a region of membrane takes relatively long, thus the long term stability of the pressure should be ensured before starting the test.
- 3) Align the experimental setup as illustrated in Section 5.2.  
Make sure that the device is firmly fixed on the working stage.
- 4) Choose autofocus mode with  $400\mu\text{m} \times 400\mu\text{m}$  observation window. Bulge the sample to 0.15 PSI. Focus on central bulged region. Resolution  $2\mu\text{m}$  in X and  $20\mu\text{m}$  in Y.

Continuous mode performs a scan without tracking the focus, therefore is faster but can handle limited height steps. Data points are lost significantly via this mode. Non-continuous (or autofocus) mode automatically tries to track the focus in the event. This gets lost from one scanning point to the adjacent one. A single scan lasts longer but this mode can handle larger height step, ideally up to 1 mm. Comparison of two modes can be seen in Fig.5.3.

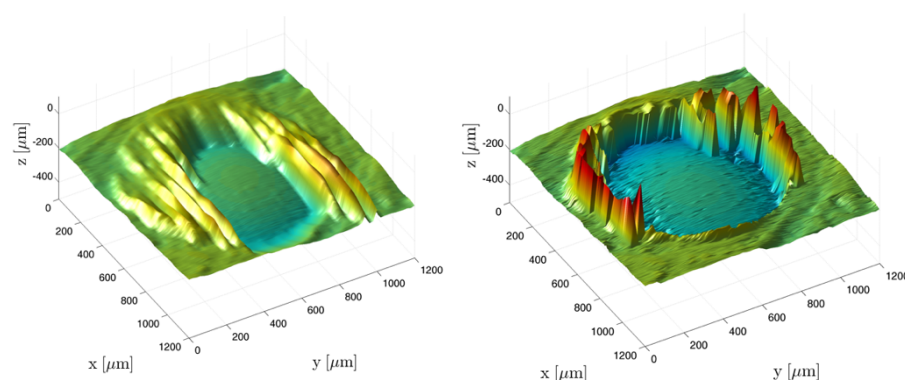


Fig.5.3. Full field of view scan with continuous mode (left, 3min) and autofocus mode (right, 30min)

However, non-continuous mode on full-field of bulge window is relatively slow, it takes around 30 min to obtain profile for a single pressure value. Nevertheless, only the mostly bulged central region is concerned to this study. By observing full field topographies in Fig.5.3, one can tell it is safe to keep observation area as  $400\mu\text{m} \times 400\mu\text{m}$  and use autofocus mode, for reducing experiment time without losing significant data points.

The interested central region cannot be located while the membrane is at rest. In order to determine the concerned region, a small pressure is applied to bulge the membrane at first. The central bulged region is obvious and thus can be locked up. The resolution is anisotropic because the profilometer is primary intended for line profile measurements. Therefore, surface measurements are actually a collection of adjacent line profiles with a specific line density.

- 5) Release the pressure to zero, obtain the first profile data, record as 0 pressure.

This is the initial data point of our experiment.

- 6) Increase pressure at interval of 0.05 PSI until it reaches 0.50 PSI, record profile for each pressure.

As we can infer from the pressure/deflection curves shown in Chapter 3, at the beginning of the test, a small increment of pressure results in considerable deflection. Therefore, experimental data points at small pressure values should be denser than at high pressure values.

- 7) Beyond 0.50 PSI, increase the pressure at interval of 0.10 PSI, until it reaches 1.00; record a height profile for each pressure.

## 5.4 Results and discussion

### 5.4.1 Data post-processing and result discussion

Once the experimental data by in-situ profilometry are available, a sequence of bulged membrane topographies can be processed for both imaging and material parameters identification purposes (see Figure 5.4). In this study, all the scripts implementing the automated post-processing procedure were developed in MATLAB (MathWorks<sup>®</sup>, US) and MATHEMATICA (Wolfram, US) programming environments.

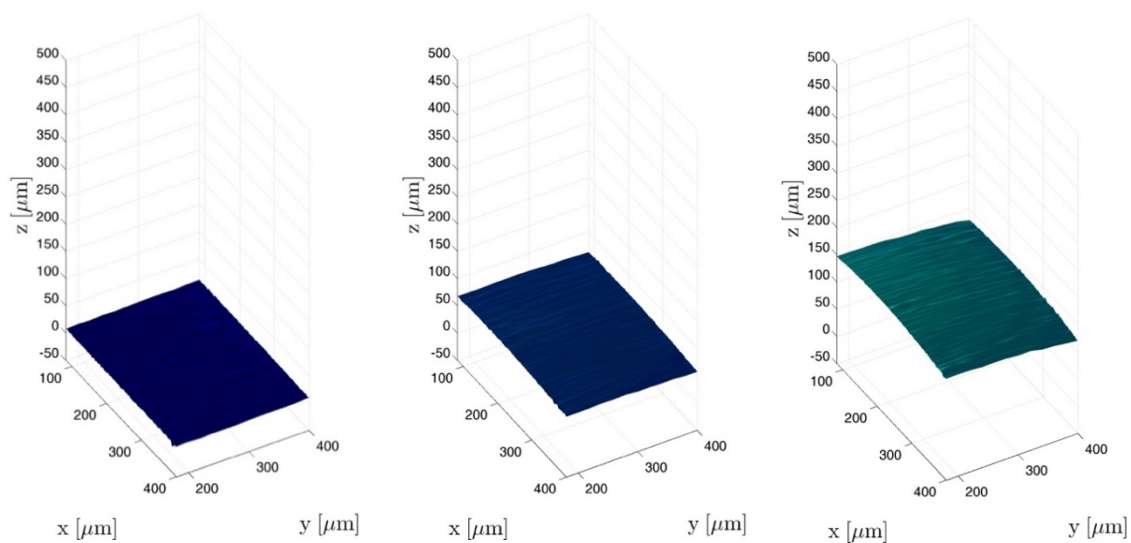


Fig.5.4. Example of synthesized topography sequence

Deflection height is the desired parameter from the topography, which can be obtained by two different post-processing method:

1. On one hand, the top of the spherical cap can be identified and the corresponding height value can be used as a measurement of the *relative* deflection. Being a direct measurement, this method inherits the level of the accuracy of the equipment itself, therefore is expected to be accurate. Nevertheless, height measurements are inherently referred to the absolute reference frame of the profilometer at the moment of the scan, therefore data can be related to each other only as long as they were acquired with reference to the very same fixed Cartesian frame. As a main drawback, this prevents the user to adjust the acquisition range in the z-direction during the experiment; therefore, great care is required when setting up the experiment, to ensure that the first topographies of the sequence lay at the bottom end of the measuring range, in order to



exploit the full range of height measurement across the test. Also, unless a precise knowledge of the  $z$ -coordinate corresponding to the non-deflected condition of the sample is available, height data can only express relative deflection increments and cannot be used directly for the purpose of describing the pressure/deflection relation, which is inherently non-linear and therefore requires absolute values of deflection.

2. Alternatively, topography data can be best-fitted by a function describing a hemispherical surface parameterized by the coordinates of the center  $(x_c, y_c, z_c)$  and the sphere radius  $(R)$ .

$$z(x, y) = z_c + (R^2 - (x - x_c)^2 - (y - y_c)^2) \dots \text{(Eq. 5.1)}$$

Recalling the trigonometric arguments expressed in equation Eq.5.1, the center deflection can be computed making use of the best-fitting radius and the bulge window characteristic dimension. The advantage of this method is that the estimation of the deflection is completely independent from the absolute reference frame used when performing the profilometry scans. This implies that the deflection history can, in principle, be reconstructed by a sequence of topographies which do not share the absolute reference frame. This is an observation of practical interest, since it means that the user is allowed to change the absolute reference acquisition by acquisition, for instance, to maximize the physical surface which will fall within the current measuring range in the  $z$ -direction. On the other hand, the estimated center deflection is sensitive to the quality of the best-fitting step. Therefore, despite the nominal accuracy of the profilometer, the reliability of the deflection estimation is expected to be relatively poor in the even of high best-fitting residuals or even divergence of the best-fitting loop.

In this work, the two aforementioned methods were combined to process the sequence of topographies. Firstly, the sequence is best-fitted with spherical surfaces, thus a sequence of fitted radius is obtained. As a reference for the details of the best-fitting function, the reader is addressed to the documentation of the *Issphere.m* function belonging to the open library on the Least Squares Geometric Elements (LSGE) for MATLAB environment [39]. An example of best fitting is shown in Fig.5.5.

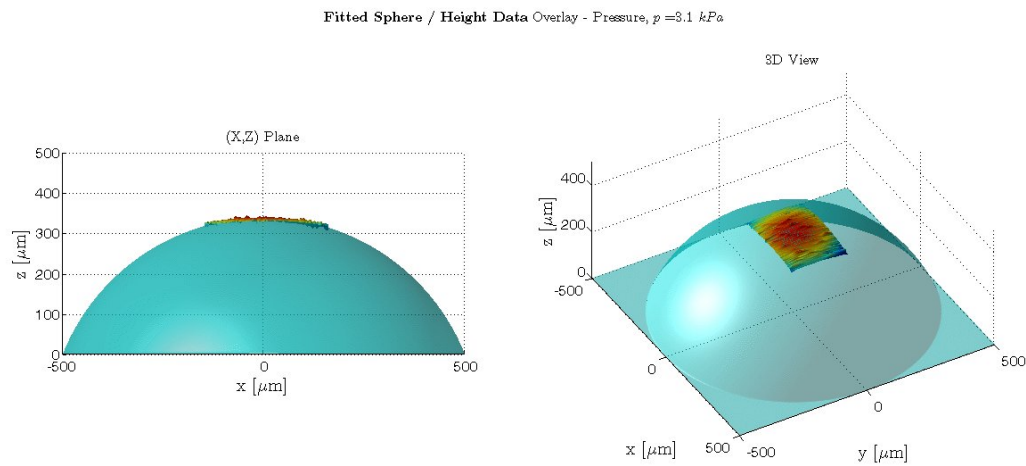


Fig.5.5. Example of best-fitting procedure

The fitted radius is then used to calculate corresponding absolute deflection height. The deflection value obtained from the first bulged membrane is then set as the reference and first value for direct height measurements. The remaining deflection height values are then obtained from the relative height from reference.

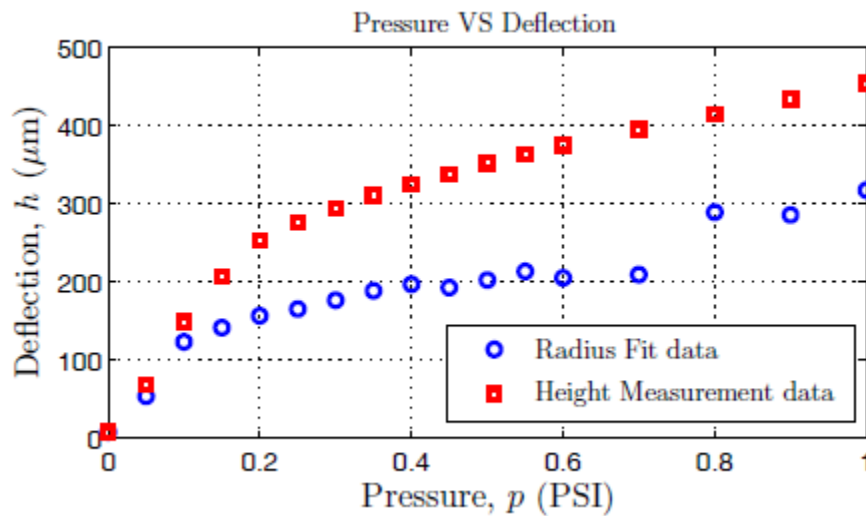


Fig.5.6. Result of radius fit data and height measurement data

Noted that, in direct measurement, the maximum deflection height was computed as the average height value in a  $20\mu\text{m}\times 20\mu\text{m}$  observation region which is at the top of the spherical cap. This area corresponds to 0.25 % of the whole imaged Field of View. The assumption is that, due to the fact that the gradient of the spherical cap surface should be approaching zero at

the top of the bulged geometry, averaging over such a small fraction of the Field of View only results in noise reduction and does not imply underestimation of the top deflection.

Fig.5.6. shows an example result of pressure-deflection behavior obtained from both method, one is purely fitted radius computing, and the other is height measurement referenced by a single radius fitted data.

As one can observe, the radius fit data shows an unfeasible tiny decline of deflection at pressure of 0.7 PSI, which might be due to inaccuracies during fitting. The height measurement data, on the other hand, show a more stable and feasible tendency of pressure-deflection correspondence which complies with the theoretical modeling. Therefore, the *height data* curve was used to estimate the strain state of the sample.

The deflection-strain conversion can be made through geometry of spherical cap model:

$$\varepsilon_{nominal} = \frac{R\theta - a}{a} \dots \dots (Eq. 5.2.)$$

$$\varepsilon_{logarithmic} = \log \frac{R\theta}{a} \dots \dots (Eq. 5.3.)$$

Where R and  $\theta$  can be referred to in Chapter 3:

$$R = \frac{a^2 + h^2}{2h} \dots \dots (Eq. 3.10)$$

$$\theta = \arcsin \frac{a}{R} \dots \dots (Eq. 3.12)$$

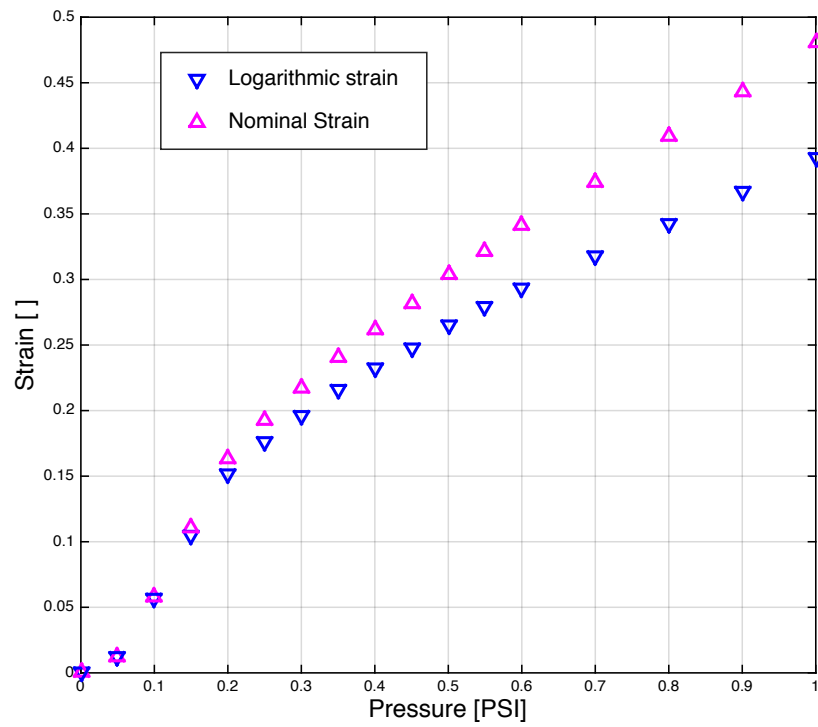


*Fig.5.7. Computed pressure/strain relation*

The computed pressure-strain relation is shown in Fig.5.7. With this pressure-strain relationship, the bulge device is now ready to be used for crack opening study under in-situ optical microscopy, which will be described in Chapter 6.

### **5.4.2 Characterization with hyperelastic model fitting**

With the experimental pressure-strain relation under in-situ laser profilometer, the strain control from the bulge test device is validated and ready to be applied in crack opening study under in-situ optical microscopy.

However, the relation illustrated in previous section is a phenomenological curve which holds for a specific bulge window size. This is a severe limitation since

1. While the extension of the profilometer measuring range is suitable for bulge window sizes not higher than 500  $\mu\text{m}$  in radius,
2. Bigger bulge windows would ensure a wider top region approaching a vanishing gradient at the top of the bulged geometry, therefore ensuring that, when imaging the bulged sample at the optical microscope, the portion of the Field of View which lays within the depth of field of the magnification objective is maximized and an overall sharper image can be obtained

Furthermore, even when the profilometry equipment were not setting any constraint of the height measuring range, performing an in-situ profilometry characterization for each bulge window size of interest would be inconveniently time consuming. Indeed, each set of laser profilometer experiments requires about 4 hours man-time work.

To address the aforementioned limitation, it is worth recalling that the pressure/strain relation can be generalized, if combined with the fitting of the hyperelastic bulge equation derived in Chapter 3. Constitutive behavior of the membrane is obtained by fitting the pressure-deflection curve to a proper hyper elastic model, thus pressure-strain relation under different window size can be predicted. That is to say, by performing a single set of experiment under laser profilometer, and fitting the result with hyper elastic bulge modeling, one can perform crack opening study under optical microscope with an arbitrary window size, irrespective of the actual dimension used when performing the in-situ profilometry experiment.

The fitting of profilometry experimental result to the hyperelastic bulge modeling also enables the characterization. Though it is not the goal of this programme, it may be useful for studies focusing on this area.

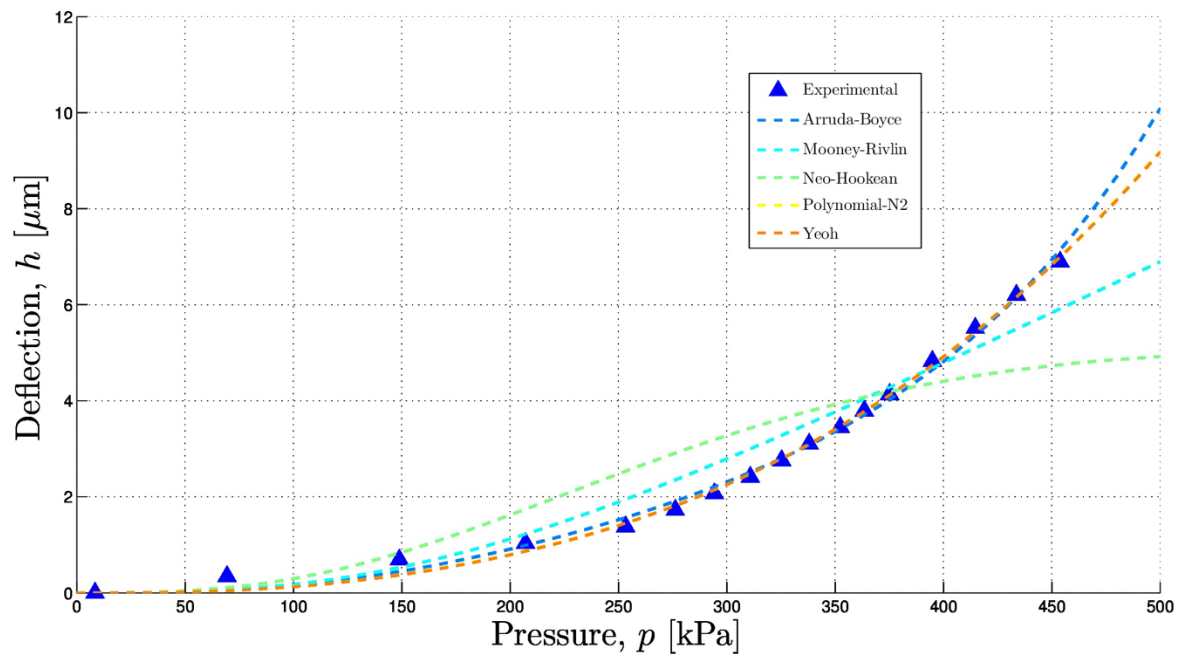


Fig.5.8. Fitting of experimental pressure-deflection curve with hyperelastic models

Fig.5.8. shows the fitting of the experimental pressure-deflection relation from previous section to different hyperelastic bulge models. The Polynomial (N=2) model and the Yeoh model provide the best results. The complete overlapping of Polynomial (N=2) and Yeoh model is due to the fact that Yeoh hyperelastic model is inherently a specific instance of the Polynomial model, thus it is not surprising to see they coincide with each other. The slight underestimation of deflection at the beginning period may be interpreted as a consequence of the poor quality of the very first data of the acquisition sequence due to a non-flat geometry of the sample at rest, which implies an *initial height* error (see Section 2.6, “Possible sources of error in bulge test”) that cannot be quantified by mean of the tools described in this work.

Experimental parameters are obtained by fitting:  $C_{10}=2.81$  kPa,  $C_{20}=1.84$  kPa,  $C_{30}=0.13$  kPa. One can reconstruct the pressure-strain relation by the Yeoh hyperelastic bulge equation in Chapter 3, merely substituting the window size with a desired one.

For the purpose of characterization, one can obtain the constitutive behavior of the sample in Yeoh form as follows:

$$\Psi = 2.81335(I_1 - 3) + 1.8441(I_1 - 3)^2 + 0.131283(I_1 - 3)^3 \dots \dots (Eq. 5.4.)$$

## 6 Bulge test with in-situ optical microscopy

It is the original objective of the whole study, to develop an experimental setup and related procedure for the in-situ mechanical characterization of the fracture behavior of Au/PDMS samples through bulge testing, where in-situ optical microscopy serves as the characterization instrument.

An inverted microscope is used in our experiment, 20X objective was the maximum magnification available. It was enough to observe crack opening evolution upon increasing pressure, i.e. increasing the strain of the sample. Crack opening was manually measured by mean of the image processing software imageJ, however it is worth mentioning that the accuracy of crack opening measurements can be improved in the future if an automatic measurement was developed.



## 6.1 Setup description

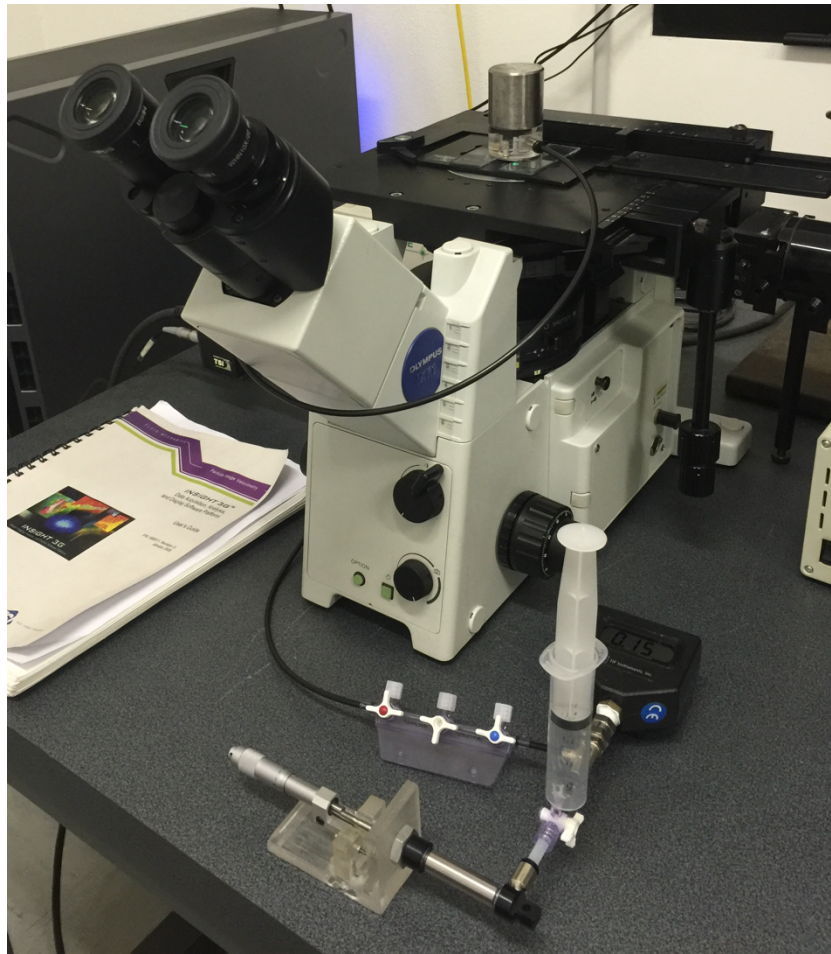


*Fig.6.2. Experimental setup for bulge test with in-situ Optical Microscopy*

The overall setup is shown in Fig.6.2.

A digital camera is mounted onto the microscopy to record in-situ images of cracks opening under bulge test. Pixel density is 2048x2048.

## 6.2 Experimental Protocol

The experiment is performed under the following protocol:

- 1) Align the bulge test setup as illustrated in Fig.4.2.2.
- 2) Align the experimental setup as illustrated in 6.2.  
Make sure that the device is firmly fixed on the stage.
- 3) Power on camera, tune light to sufficient luminance, locate the bulge window.  
An in-situ monitoring is achieved by camera using continuous capturing mode, i.e., the screen is updated continuously. The circular window center should be around the center of monitoring screen.
- 4) Start taking images at zero pressure under each magnification, increase pressure at interval of 0.05 PSI until it reaches 0.5 PSI, afterwards increase pressure at interval of 0.1 PSI, capture images.
  - The sequence used to study cracks opening evolution is under 20X magnification.
  - Once the membrane is bulged, the user should try to re-center the image, putting the bulged center as center of the observation view.
  - A concentric blurring can be seen while tuning the focus in and out. The center of the blurring is the most bulged center of the membrane. The user should adjust the stage gently to let the bulged center coincide with the image center. In this manner, the most strained region will be imaged and ready for further study.
  - Record the sequence and the corresponding pressure.
- 5) Export images, close the operation software, turn down illumination, unplug camera power, demount the bulge test device.

### 6.3 Results and discussion

The experiment is performed under two different window size, one is 1mm in diameter, the other is 2mm. Two segment of result image sequence for both window sizes are shown below.

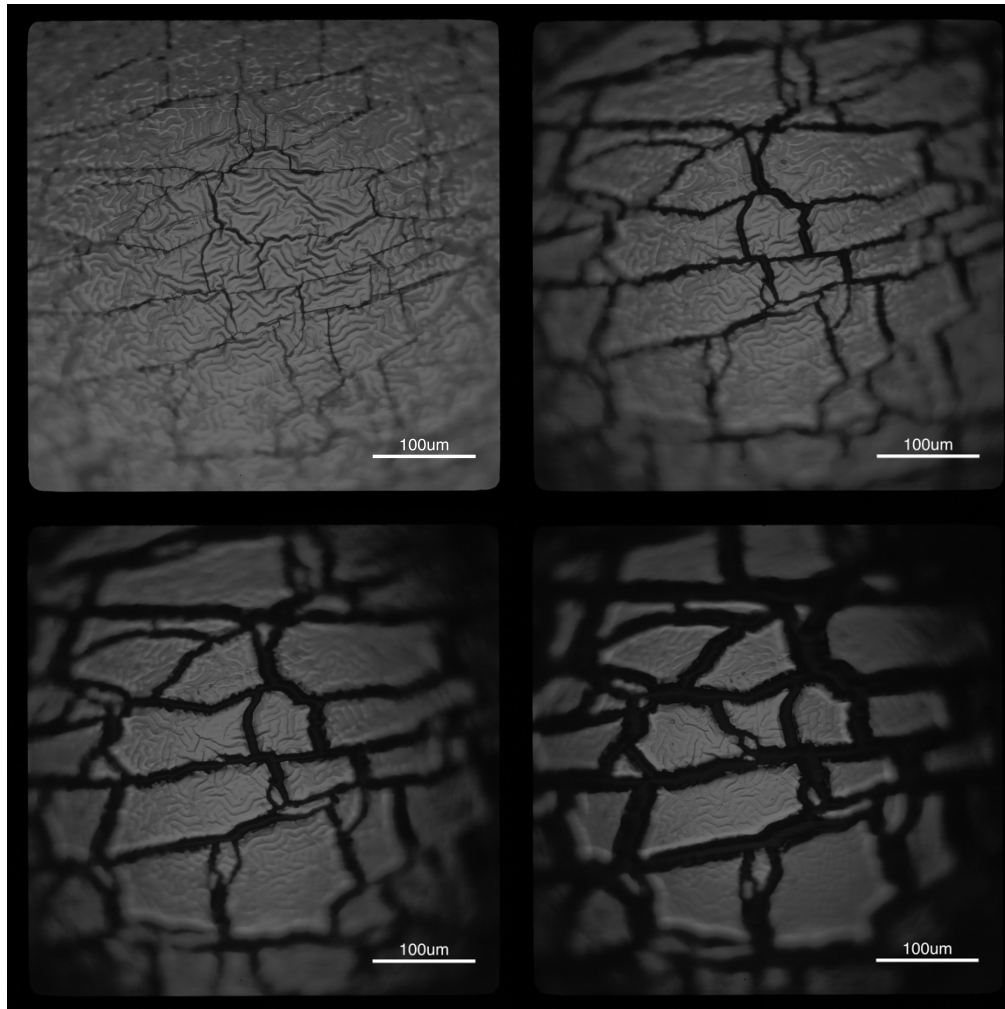


*Fig.6.3. Segment of result image sequence for bulge test under in-situ Inverted Microscope. ( $a=500\mu\text{m}$ )*

The crack opening appearances are relatively different for two cases. As predicted from the bulge equation, same pressure will lead to higher deflection, thus higher strain state, corresponding to a larger window size. That is to say, cracks will be larger under same applied pressure, if window size is larger.

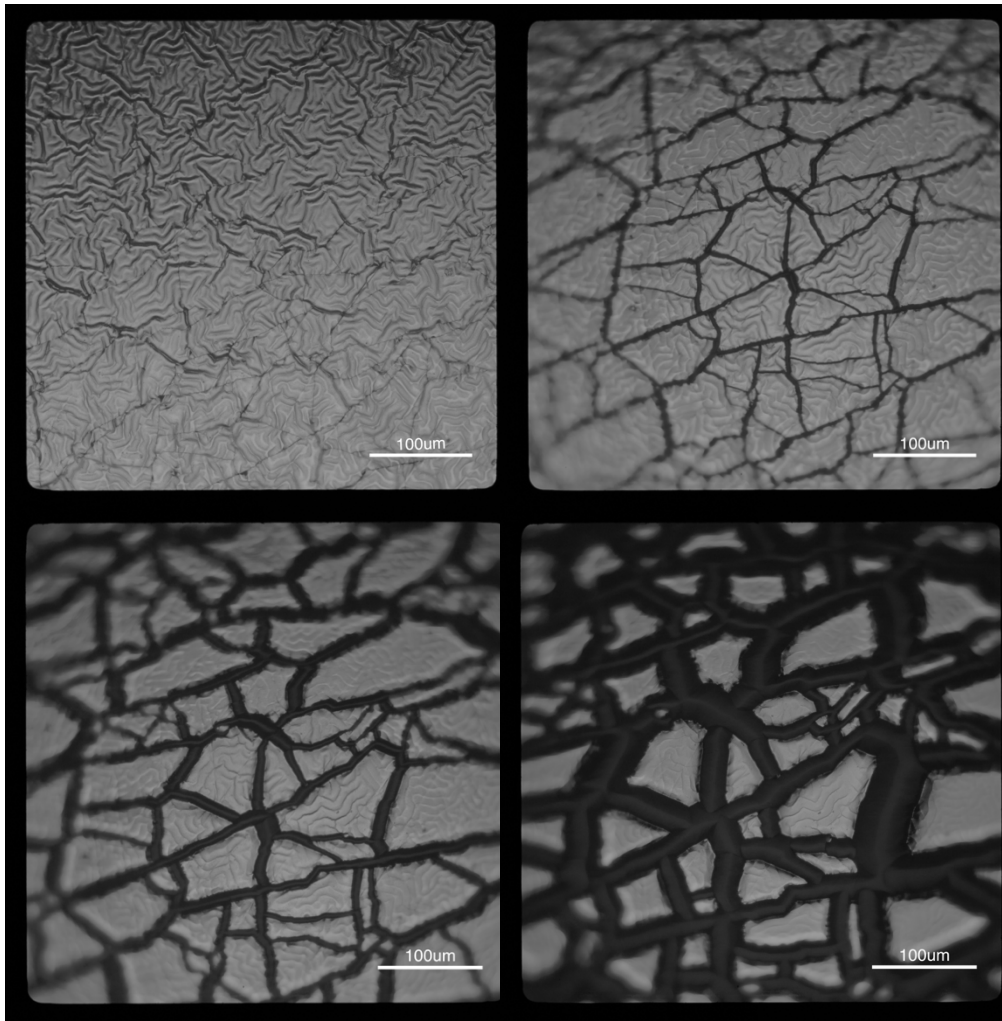


*Fig.6.4. Segment of result image sequence for bulge test under in-situ Inverted Microscope. ( $a=1000\mu\text{m}$ )*

When comparing the optical micrographs by the two experiments, it can be noticed that a larger in-focus region, which is more interesting in crack opening study, can be observed with a larger window size. It provides more cracks available for further study, while in the smaller window case, a smaller in-focus region can only provide limited numbers of clear cracks.

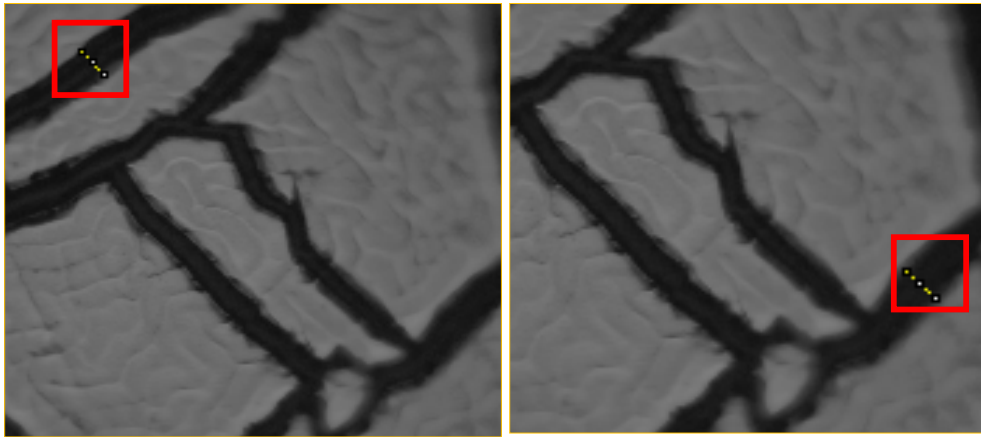


*Fig.6.5. Simple illustration of post-processing of image sequence: crack measuring in ImageJ*

For these reasons, a larger window radius is more applicable as far as a crack opening study is concerned. But the latter is not applicable for in-situ profilometry experiments, where the strain control mechanism, that is, pressure/strain relation, is obtained. The working distance of the laser profilometer used in this project makes it unsuitable to attempt experiments in which the bulge window size is higher than 500  $\mu\text{m}$ . Thus, for larger window which may have deflection larger than 500 $\mu\text{m}$ , the full range pressure-deflection relation cannot be obtained. A direct pressure-deflection behavior, or more explicitly, a pressure-strain behavior, is not available from experiment with in-situ profilometry, for window size larger than 500 $\mu\text{m}$ .

That is to say, for determination of strain control under profilometer, a window with 500 $\mu\text{m}$  in radius is more desired, while in the crack opening study, a larger window is preferred. Hyperelastic bulge modeling can be used to address this need. A detailed illustration with corresponding result will be shown later.

Crack opening study is conducted by measuring a crack opening distance using ImageJ manually, and record data with respect to corresponding applied pressure. Cracks from the most interested region - bulged region are studied. A simple illustration can be seen in Fig.6.5. Several cracks are measured within a single image to yield an average crack opening range instead of a single data that may be hugely dependent on measurement accuracy. The cracks opening distance are related to applied pressure. An example result of crack opening measurement is shown in Fig.6.6.

In Fig.6.6. experimental results for both window size ( $a=500\mu\text{m}$  and  $a=1000\mu\text{m}$ ) are shown. The difference between the two curves confirms that the relation between crack opening and pressure is window size dependent. A pure applied pressure value does not give any information on the strain state of the membrane and thus is not satisfactory for crack opening study. To better interpret the result, one should refer to the pressure/strain relation, which is obtained from experiment under laser profilometer and fitted with the hyperelastic bulge modeling.

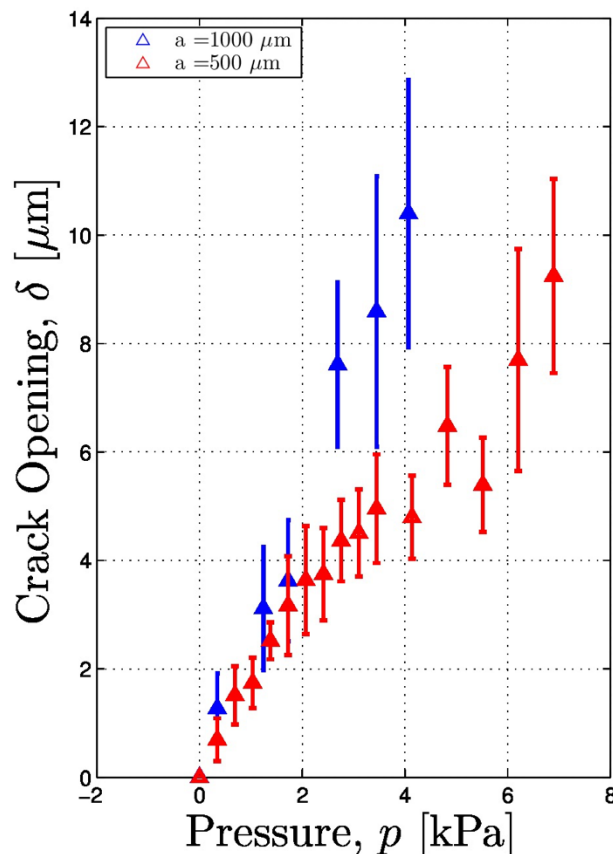


Fig.6.6. Crack opening VS Pressure for both window size

One can perform profilometry experiment using a cap with window size  $500\mu\text{m}$ , and fit the experimental pressure-deflection relation to hyper elastic bulge equation for different models. A best-fit model then can provide material parameters to construct the constitutive behavior of the substrate material. The best-fit set of material parameters then is used in hyperelastic bulge equation for a different, larger window size, which is more preferred in crack opening study with in-situ optical microscopy. A different pressure-deflection behavior is thus predicted. The new predicted pressure-deflection behavior is used to yield the pressure-strain relation through

geometry control of spherical cap model. At last, the crack opening-pressure relation can be converted into crack opening-strain relation, which is more meaningful desired in crack opening study.

Fig.6.7. shows the computed relation between crack opening distance and strain for both window size ( $a=500\mu\text{m}$  and  $a=1000\mu\text{m}$ ). The two sets of experimental data collapse to each other, while in Fig.6.6 they split with respect to pressure. The results show the independence on window size of the crack opening evolution corresponding to increasing strain, which coincide with general crack opening behavior of the material. This result can prove that the experimental setup developed in this project can be used in crack opening study of metal thin film on polymer substrate.

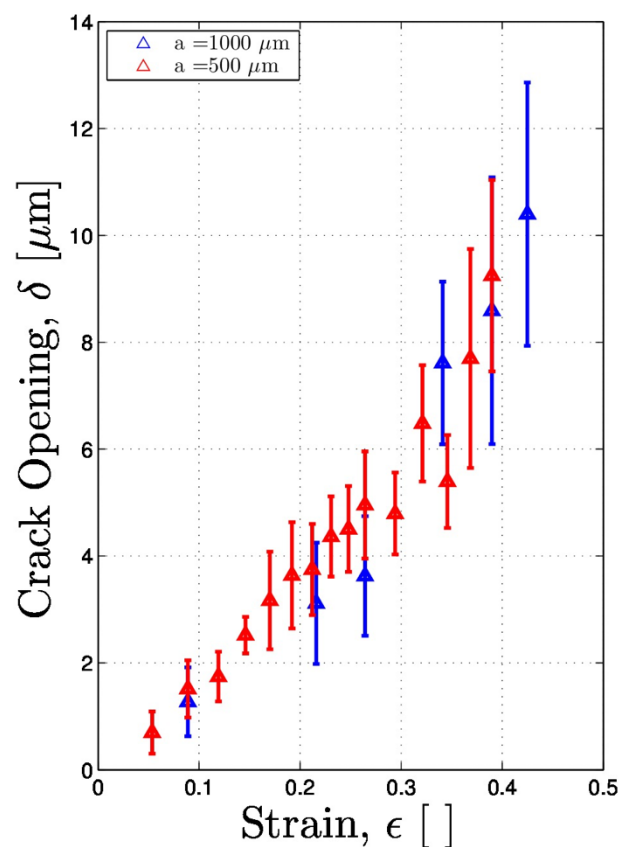


Fig.6.7. Computed Crack opening VS Strain for both window size



## 7 Conclusion and Recommendations

### 7.1 Thesis Conclusion

This thesis is about the development of an experimental setup for the in-situ mechanical characterization of metal thin films on polymer substrates through bulge testing.

In the first chapter, basics of stretchable electronics are introduced. Gold on PDMS is one of the most popular configuration for stretchable electronics studies, and it is the main sample used in this programme. Chapter 1 also illustrates the material choice.

In Chapter 2, theoretical principles of bulge test are presented. The derivation of bulge equations for different window shapes is illustrated. The bulge equations are constructed mainly for linear elastic materials, which does not comply to the used sample for stretchable electronics in this programme.

In Chapter 3, under assumption that mechanical properties mainly depend on PDMS, constitutive behavior of the polymer is considered as an affecting factor for bulge equation. Hyperelastic bulge modeling is constructed, bulge equation is rewritten into hyperelastic forms, taking into consideration of polymer properties. Several constitutive hyperelastic models are used to build up the hyperelastic bulge equation: Arruda-Boyce form, Mooney-Rivlin form, Neo-Hookean form, Polynomial form and Yeoh form.

In Chapter 4, the manufacturing procedure of the bulge test device and the experimental setup are illustrated in details. The setup uses air as pressure source, syringe and micrometric screw as compressor to build up pressure. Cap and chamber are specially designed and fabricated under the consideration of practicality and good quality of sealing.

In Chapter 5, bulge test with in-situ laser profilometry is illustrated. Setup is described, experiment protocol is presented. The goal of bulge test experiment under profilometer is to obtain the pressure/strain relationship of the sample, such that the mechanism can be applied to crack opening study under optical microscopy. But the experiment setup can be used also for characterization of metal thin films on polymer substrates, combining hyperelastic bulge equation modeling. An example of the experiment and the result is presented in this chapter,



indicating the feasibility to use this setup for both the identification of the pressure/strain relationship and the mechanical characterization of the material.

In Chapter 6, bulge test under in-situ optical microscopy is illustrated. Setup is described, experiment protocol is presented. It is the goal of this project, to study crack opening of metal thin film on polymer substrate, example experiment result shows the feasibility to achieve this goal through the experiment setup developed in this programme.

In Chapter 7, thesis conclusion will be presented to summarize up the whole outline of the thesis. Conclusion outline of the experimental setup for the in-situ mechanical characterization of metal thin films on polymer substrates through bulge testing is presented. Advantages and disadvantages of the in-situ laser profilometry and optical microscopy are discussed briefly. At last, recommendations and future perspectives are discussed.

## 7.2 Conclusion on the experimental setup

The main target of this project is to conduct crack opening study of gold on PDMS through bulge test. A detail fabrication procedure of the bulge device and its pressure providing and controlling components are illustrated in Chapter 4. The bulge test should be setup under the guidance in Chapter 4 before further usage under in-situ experimental instruments.

The aligned bulge test setup is then used in combination with a laser profilometer, under experimental guidance in Chapter 5. A  $400\mu\text{m}\times 400\mu\text{m}$  observation region is determined, under autofocus mode, to obtain adequate data points within reasonable time. The laser profilometry yields result as sequence of topographies corresponding to increasing bulge pressure. To post-process the result, topographies are first chopped into smaller region to get rid of noise which typically appears at the edges of the profile due to the limited capability of the setup to cope with surfaces at an angle higher than  $15^\circ$ ; then best fitted in Matlab with a spherical cap surface. Fitted deflection height is calculated through fitted radius values. The first fitted deflection height is used as the reference of direct height measurement, and the lateral deflection height is obtained with respect to this reference. The pressure-deflection relation is obtained using post-processed experimental data. It can be fitted with hyperelastic bulge equation derived in Chapter 3, such that material parameters are known. With this set of parameters, either material characterization, or prediction of pressure/deflection behavior with different window size can be achieved. Once the pressure/deflection behavior is known, either experimentally or by best fitting, the result can be used to express the crack opening evolution (imaged by means of in-situ optical microscopy) with respect to the strain rather than the chamber pressure under in-situ optical microscopy.

With the known strain control mechanism, the aligned bulge test setup is ready to be used under optical microscope under experimental guidance in Chapter 6. 20X objective was the magnification level to focus on. The image sequences are post-process using ImageJ. Crack opening is measured manually as increasing displacement under increasing applied pressure. Pressure is converted into strain using the pressure-strain relation obtained in profilometer.

### **7.3 Advantages and disadvantages of in-situ laser profilometry and in-situ optical microscopy**

#### **In-situ laser profilometry**

In-situ profilometry experiment of bulge test can give topographies under each pressure value directly. It yields intuitive results that can be interpreted in different ways. Deflection height of the bulged membrane is easily obtained, as long as a proper common reference frame is set.

But without a reference, all measured height data are only relative values that are not useful in the bulge study. Setting this reference is not an easy task. A radius fitted data point is used as the reference, which reduces a bit the intuition of the result. A full-field autofocus scanning is relatively time consuming, so the observation view is focused on the mostly bulged region. The interested region is detectable only when the membrane is already bulged. This increases the complexity of experimental operation. The experiment also has strict limitation on the device features: leakage should be completely avoided, the window size should be small enough to yield deflection height within the working distance.

#### **In-situ optical microscopy**

In-situ optical microscopy experiment of bulge test can give images of crack opening under each pressure directly. Crack opening quantification is rather convenient by conducting direct measurement of the intuitive cracks on the images.

However, the accuracy of the result depends hugely on the precision of manual measurement conducted by the user, which induce uncertainty thus affecting the result reliability.

## 7.4 Recommendation and future perspectives

The final result in Chapter 6 on the crack opening study of gold on PDMS shows the feasibility of the experimental setup developed in this thesis to be used for the purpose of crack opening study. The experimental setup can be better improved by developing the pressure providing system with a more sensitive sensor linked to PC that can monitor and control a micro-step syringe to compress or release air. The valves can be fabricated with metal instead of plastic, to give even better sealing.

An automatic quantification of crack spacing with respect to strain level can be developed, as next step of crack opening study under optical microscopy through bulge test. That would provide a mean not to introduce measurement inaccuracies inherited by the p

The results in Chapter 6 also prove the reliability of the hyperelastic bulge modeling developed in this thesis. Thus the bulge test device under in-situ profilometry can be used as an alternative method for characterization of thin film mechanical properties. Results are obtained from fitting the hyperelastic bulge equations.

With the usage of hyperelastic modeling from Chapter 3, crack opening study can also be conducted combining a uniaxial tensile test and optical microscopy observation. Fitting the result from uniaxial tensile test to hyperelastic models also gives material parameters, which can be used to construct the hyperelastic bulge equations. In such way, strain control mechanism upon the exactly same material can also be known, not from the bulge test with in-situ profilometry, but from uniaxial tensile test. Crack opening study can then be conducted in such manner. It saves more time, comparing to laser profilometer, but since the behavior in equi-biaxial stress conditions would be then computed rather than measured, the level of uncertainty in the prediction of the pressure/deflection behavior would be higher as compared to the case in which the material parameters are estimated by fitting experimental data on the equi-biaxial stress response directly.

## Bibliography

- [1] Rogers J A, Someya T, Huang Y. Materials and mechanics for stretchable electronics[J]. *Science*, 2010, 327(5973): 1603-1607.
- [2] Mata A, Fleischman A J, Roy S. Characterization of polydimethylsiloxane (PDMS) properties for biomedical micro/nanosystems[J]. *Biomedical microdevices*, 2005, 7(4): 281-293.
- [3] Lacour S P, Wagner S, Huang Z, et al. Stretchable gold conductors on elastomeric substrates[J]. *Applied physics letters*, 2003, 82(15): 2404-2406.
- [4] Bowden N, Brittain S, Evans A G, et al. Spontaneous formation of ordered structures in thin films of metals supported on an elastomeric polymer[J]. *Nature*, 1998, 393(6681): 146-149.
- [5] B efahy S, Lipnik P, Pardo en T, et al. Thickness and elastic modulus of plasma treated PDMS silica-like surface layer[J]. *Langmuir*, 2009, 26(5): 3372-3375.
- [6] Xiang Y, Li T, Suo Z, et al. High ductility of a metal film adherent on a polymer substrate[J]. *Applied Physics Letters*, 2005, 87(16): 161910.
- [7] Lambrecht N, Pardo en T, Yunus S. Giant stretchability of thin gold films on rough elastomeric substrates[J]. *Acta Materialia*, 2013, 61(2): 540-547.
- [8] Kim D H, Lu N, Ma R, et al. Epidermal electronics[J]. *science*, 2011, 333(6044): 838-843.
- [9] Sharpe Jr W N, Yuan B, Edwards R L. A new technique for measuring the mechanical properties of thin films[J]. *Microelectromechanical Systems, Journal of*, 1997, 6(3): 193-199.
- [10] Yeoh O H. Some forms of the strain energy function for rubber[J]. *Rubber Chemistry and technology*, 1993, 66(5): 754-771.
- [11] Garnier F, Hajlaoui R, Yassar A, et al. All-polymer field-effect transistor realized by printing techniques[J]. *Science*, 1994, 265(5179): 1684-1686.
- [12] Sun Y, Rogers J A. Inorganic semiconductors for flexible electronics[J]. *ADVANCED MATERIALS-DEERFIELD BEACH THEN WEINHEIM-*, 2007, 19(15): 1897.
- [13] Cao Q, Rogers J A. Ultrathin Films of Single-Walled Carbon Nanotubes for Electronics and Sensors: A Review of Fundamental and Applied Aspects[J]. *Advanced Materials*, 2009, 21(1): 29-53.
- [14] Roncali J, Leriche P, Cravino A. From One-to Three-Dimensional Organic Semiconductors: In Search of the Organic Silicon?[J]. *Advanced materials*, 2007, 19(16): 2045-2060.

- [15] Reese C, Bao Z. Organic single-crystal field-effect transistors[J]. *Materials Today*, 2007, 10(3): 20-27.
- [16] Sekitani T, Noguchi Y, Hata K, et al. A rubberlike stretchable active matrix using elastic conductors[J]. *Science*, 2008, 321(5895): 1468-1472.
- [17] Sekitani T, Nakajima H, Maeda H, et al. Stretchable active-matrix organic light-emitting diode display using printable elastic conductors[J]. *Nature materials*, 2009, 8(6): 494-499.
- [18] Baca A J, Ahn J H, Sun Y, et al. Semiconductor Wires and Ribbons for High-Performance Flexible Electronics[J]. *Angewandte Chemie International Edition*, 2008, 47(30): 5524-5542.
- [19] Kim D H, Xiao J, Song J, et al. Stretchable, curvilinear electronics based on inorganic materials[J]. *Advanced Materials*, 2010, 22(19): 2108-2124.
- [20] Mata A, Fleischman A J, Roy S. Characterization of polydimethylsiloxane (PDMS) properties for biomedical micro/nanosystems[J]. *Biomedical microdevices*, 2005, 7(4): 281-293.
- [21] Wagner S, Lacour S P, Jones J, et al. Electronic skin: architecture and components[J]. *Physica E: Low-dimensional Systems and Nanostructures*, 2004, 25(2): 326-334.
- [22] Sharpe Jr W N, Yuan B, Edwards R L. A new technique for measuring the mechanical properties of thin films[J]. *Microelectromechanical Systems, Journal of*, 1997, 6(3): 193-199.
- [23] Ogawa H, Suzuki K, Kaneko S, et al. Measurements of mechanical properties of microfabricated thin films[C]//*Micro Electro Mechanical Systems, 1997. MEMS'97, Proceedings, IEEE., Tenth Annual International Workshop on. IEEE, 1997: 430-435.*
- [24] nix note
- [25] Li X, Bhushan B. A review of nanoindentation continuous stiffness measurement technique and its applications[J]. *Materials characterization*, 2002, 48(1): 11-36.
- [26] Oliver W C, Pharr G M. An improved technique for determining hardness and elastic modulus using load and displacement sensing indentation experiments[J]. *Journal of materials research*, 1992, 7(06): 1564-1583.
- [27] Hencky H. Uber den Spannungszustand in kreisrunden Platten mit verschwindender Biegesteifigkeit[J]. *Zeitschrift fur Mathematik und Physik*, 1915, 63(311): 311-317.
- [28] Beams J W. Mechanical properties of thin films of gold and silver[J]. *Structure and properties of thin films*, 1959: 183-192.
- [29] Tsakalakos T. The bulge test: a comparison of the theory and experiment for isotropic and anisotropic films[J]. *Thin solid films*, 1981, 75(3): 293-305.
- [30] Small M K, Nix W D. Analysis of the accuracy of the bulge test in determining the

- mechanical properties of thin films[J]. *Journal of Materials Research*, 1992, 7(06): 1553-1563.
- [31] Vlassak J J, Nix W D. A new bulge test technique for the determination of Young's modulus and Poisson's ratio of thin films[J]. *Journal of Materials Research*, 1992, 7(12): 3242-3249.
- [32] Pratt R I, Johnson G C. Mechanical characterization of thin films using full-field measurement of diaphragm deflection[C]//*MRS Proceedings*. Cambridge University Press, 1993, 308: 115.
- [33] Tabata O, Kawahata K, Sugiyama S, et al. Mechanical property measurements of thin films using load-deflection of composite rectangular membrane[C]//*Micro Electro Mechanical Systems, 1989, Proceedings, An Investigation of Micro Structures, Sensors, Actuators, Machines and Robots*. IEEE. IEEE, 1989: 152-156.
- [34] R. Donders, Master Thesis, 2015.
- [35] Bonet J, Wood R D. *Nonlinear continuum mechanics for finite element analysis*[M]. Cambridge university press, 1997.
- [36] Tinku S, Collini C, Lorenzelli L, et al. Smart contact lens using passive structures[C]//*SENSORS, 2014 IEEE*. IEEE, 2014: 2107-2110.
- [37] Tinku S, Bartali R, Dahiya R, et al. *Characterisation of Gold Patterns on PDMS Substrates*[M]//*Sensors*. Springer International Publishing, 2015: 255-258.
- [38] Stemp W J, Stemp M. UBM laser profilometry and lithic use-wear analysis: a variable length scale investigation of surface topography[J]. *Journal of Archaeological Science*, 2001, 28(1): 81-88.
- [39] Eurometros.org,. 2015. 'LSGE: The Least Squares Geometric Elements Library Consists Of Matlab Functions To Find ...'.  
[http://www.eurometros.org/gen\\_report.php?category=distributions&pkey=14&subform=yes](http://www.eurometros.org/gen_report.php?category=distributions&pkey=14&subform=yes).